Univerzita Karlova v Praze
Matematicko-fyzikální fakulta

DIPLOMOVÁ PRÁCE

Filip Kostka

Dynamické modely zemětřesného zdroje a seismicita

Katedra geofyziky

Vedoucí diplomové práce: RNDr. František Gallovič, Ph.D.

Studijní program: Fyzika

Studijní obor: Geofyzika

Praha, 2015

Tato práce vznikla za finanční podpory grantové agentury Univerzity Karlovy pod projekty SVV-260218 a GAUK 2032214.

Prohlašuji, že jsem tuto diplomovou práci vypracoval samostatně a výhradně s použitím citovaných pramenů, literatury a dalších odborných zdrojů. Beru na vědomí, že se na moji práci vztahují práva a povinnosti vyplývající ze zákona č. 121/2000 Sb., autorského zákona v platném znění, zejména skutečnost, že Univerzita Karlova v Praze má právo na uzavření licenční smlouvy o užití této práce jako školního díla podle §60 odst. 1 autorského zákona.

V Praze dne 31.7.2015 Filip Kostka

Contents

Název práce: Dynamické modely zemětřesného zdroje a seismicita
Autor: Filip Kostka
Katedra: Katedra geofyziky
Vedoucí bakalářské práce: RNDr. František Gallovič, Ph.D., katedra geofyziky

Abstrakt:
Předmětem práce je modelování zemětřesného zdroje pomocí tzv. rate-and-state zákonů tření vycházejících z laboratorních měření. V jazyce Fortran 90 jsme napsali jsme kód pro modelování rovinného, obecně nakloněného dvojrozměrného zlomu s heterogenním rozložením parametrů tření, ponořeného v nekonečném elastickém poloprostoru. Model používáme v tzv. kvazidynamické aproximaci. Pomocí něj provedeme velké množství numerických experimentů na prozkoumání vlivu rozložení parametrů tření na časoprostorovou komplexitu skluzu na zlomu. Dále zkoumáme vliv změny tzv. Coulombova napětí na změny načasování příchodu zemětřesení. To aplikujeme na model homogenního zlomu i na model s náhodným rozložením třecích parametrů, jehož seismicita vykazuje Gutenberg-Richterovo chování na rozsahu dvou magnitud. Zjišťujeme, že vliv změny Coulombova napětí je netriviální a závisí mj. na pozici namáhané oblasti a rychlosti skluzu na ní.

Klíčová slova: Zemětřesení; Dynamický model; Seismicita

Title: Dynamic models of earthquake source and modeling of seismicity
Author: Filip Kostka
Department: Department of Geophysics
Supervisor: RNDr. František Gallovič, Ph.D., Department of Geophysics
Abstract: In the present thesis we perform modeling of earthquake source using laboratory derive rate-and-state laws of friction. We have developed a code in Fortran 90 for modeling a planar, two-dimensional fault with general dip and heterogeneous distribution of frictional parameters. We use a quasi-dynamic approximation and assume that the fault is submerged in an infinite elastic half-space. We performed an extensive number of numerical experiments to study the effect of frictional parameters distribution on the spatio-temporal complexity of slip on fault. We also study the effect of the so called Coulomb stress changed on clock advance and clock delay of events. For this purpose we use both a homogeneous model and a model of random frictional parameters which exhibits the Gutenberg-Richter frequency-size dependence in the range of two magnitudes. We find that the effect of Coulomb stress change is nontrivial and depends on factors such as the domain of stress load and the slip velocity on it.

Keywords: Earthquake; Dynamic model; Seismicity

Introduction

There are two basic approaches to modeling earthquakes: kinematic, in which it is assumed that the spatio-temporal evolution of slip on a fault is known, and dynamic, in which physical laws are used to evaluate the evolution of slip on faults. The prevalent approach to dynamic modeling is to simulate earthquake rupture as frictional sliding. A non-linear model called *rate-and-state* friction based on laboratory experiments with sliding of rocks is most commonly used for this purpose. Rate-and-state models allow modeling of a wide range of both seismic and aseismic phenomena. In this thesis, we use frictionally heterogeneous three-dimensional models of faults governed by rate-and-state friction to explore two areas of interest: the effect of external stress applications timing of earthquake rupture and the relation between heterogeneity of frictional parameters and seismicity

Observations suggest that when stress on a fault changes - for example due a nearby earthquake- a quantity called Coulomb stress change ΔCS, plays an important role in determining the time of occurrence of subsequent earthquakes in the affected area. Coulomb stress change is defined

$$\Delta CS = \Delta\tau - \mu\Delta\sigma,$$

where $\Delta\tau$ and $\Delta\sigma$ are changes in shear and normal stress, respectively, and μ is the coefficient of friction. Areas with positive ΔCS show increased seismicity, whereas areas with negative ΔCS show a decrease in seismicity. The effect of ΔCS was explored by Perfettini et al. (2003) for a model of two-dimensional rate-and-state friction fault and Gallovič (2008) for three-dimensional fault. In this thesis, we present a study on the effect of various parameters of Coulomb stress change on the timing of earthquakes.

In order to be able to evaluate the effect of Coulomb stress change on realistic models, we search for distributions of frictional parameters that give rise to realistic Gutenberg- Richter frequency-size distribution of earthquake events. We perform these studies in a so called *quasi-dynamic* approximation, which neglects propagation of wave effects, but admits fast computation of slip on fault. Lapusta (2000) has shown that approximation does not cause major departures from the fully dynamic model

In the first chapter, we provide a brief historic review of friction, the motivation for developing rate-and-state friction, its basic properties and relevance to earthquake modeling. In the second chapter, we present the numerical methods used in this thesis. In chapter three, we show the results of our study of seismicity. In the final chapter, we show a study of the effect of Coulomb stress change on both a frictionally homogeneous model and models with heterogeneous distribution of parameters.

Chapter 1

Theoretical background

In this chapter, we explain the relevance of friction for earthquakes and present the framework of rate-and-state friction and its application to earthquake modeling.

1.1 Why friction?

For the first half of the 20th century, earthquakes were understood to arise as a result of brittle fracture in the crust. This view was first put forth by H.F.Reid after the great earthquake in San Francisco, 1906 (Zobeck, 2006) , in his theory of elastic rebound. According to this theory, the tectonic plates moving relative to each other get locked at brittle plate boundaries. As a result, elastic shear strain is gradually accumulated until the internal strength of rocks is reached and a shear crack appears, suddenly releasing the accumulated strain and stress-strain energy. The resulting slip then radiates seismic waves. On the other hand, the style of deformation below the brittle layer is dominated by ductile flow and no fracture can occur there. The theory thus provides a plausible mechanism for earthquake nucleation, as well as a causal relation between earthquakes and the formation of cracks - before its formulation, it was speculated that cracks are formed as a result of earthquakes, not the other way around - and it allows to separate lithosphere into seismic and aseismic domains. The elastic rebound theory emphasizes the importance of brittle rheology and the concept of rock strength for earthquake nucleation.

However, elastic rebound as a universal mechanism for earthquakes was challenged on several grounds. Most obviously, the theory does not explain the emergence of earthquakes on plate surfaces that are already fractured (i.e. pre-existing faults). Brace and Byerlee (1966), referring to earlier works by Jeffreys, Orowan and Griggs and Handin pointed out that rupture must be accompanied by sliding to release energy and that this sliding cannot take place because the stress drop required to overcome dry friction on the fracture surface would be prohibitively high. Another problem for elastic rebound were the low val-

ues of the stress drops estimated for most earthquakes when compared to the stress drops observed for ruptures of rocks in laboratory (the latter was typically observed to be by one ore two orders of ten higher than the former).

Brace and Byerlee suggested that the mechanism of earthquakes may be analogous to the motion of rocks sliding one over another when subjected to loading in laboratory. Rather than sliding smoothly, the rocks exhibit a kind of jerky motion called *stick-slip* (a term previously used within the engineering community) for certain laboratory conditions. During stick-slip, the rocks first undergo zero (or negligible) slip. After some time, the rocks slip suddenly and then get locked again. As long as there's loading, this motion repeats ad infinitum. This suggests that it does not arise due to the formation of cracks, but due to the dynamics of sliding friction between the rocks. We shall give a brief account of the stick-slip phenomenon in one of the following sections. Brace and Byerlee proposed that if stick-slip occurred on real geological faults, then it could provide a mechanism for earthquake nucleation on surfaces that are already fractured. It could also explain the weak stress drops and why they correspond to only a small fraction of the rock strength. Moreover, it was observed that the properties of the stick-slip motion depend not only on the characteristics of the sliding material, but also on the coupling of this material to loading. For example, by increasing the stiffness of loading or its velocity, stick-slip can be made to disappear and stable sliding occurs. This suggested that the dynamics of the stick-slip earthquakes could be studied as a system dependent stability problem, with seismic behavior occurring in the unstable stick-slip regime and aseismic behavior occurring in the stable regime. It became clear that a detailed study of friction would be necessary to understand the physics of earthquakes.

1.2 Why rate-and-state friction?

The exact micro-physical mechanism of friction remains enigmatic to this day. A brief account of history of friction physics was given by Nordhagen (2003). The first person academically interested in friction was Leonardo da Vinci. He suggested that sliding friction was proportional to the normal force and independent of the area of contact between sliding surfaces. He also introduced the concept of the coefficient of friction (ratio between the tangential and normal forces). Da Vinci's conclusions were later rediscovered by Amontson (1699), Coulomb (1785) and Morin (1833). Today, they are called Amontons' first and second law, respectively. The third Amontons' law, also known as Coloumb's law of friction, posits that the coefficient of *kinetic* friction is independent of the sliding velocity. Under Coloumb's model of friction a *static* coefficient of friction is also introduced as a threshold ratio between applied and normal force required for sliding to occur.

The first plausible microscopic explanation of the first and second Amontsons' laws was given by Bowden and Tabor in 1950 . They found that two materials sliding over another do not touch over their whole area A , but only at a small number of *asperities*, whose real area is A_r. Bowden and Tabor as-

sume that both the macroscopic normal force N and the frictional force F are proportional to the real contact area, so that that

$$N = A_r\sigma_c, \qquad F = A_r\tau_c,$$

where σ_c and τ_c are the contact stresses at asperities. These relations follow from assuming that the asperities undergo plastic deformation, so σ_c and τ_c correspond to plastic yield stress of asperity junctions (Putelat, 2011). For the coefficient of friction μ , this implies

$$\mu = \frac{F}{N} = \frac{\tau}{\sigma} = \frac{\tau_c}{\sigma_c}, \tag{1.1}$$

which is independent of the area and normal force. The adhesive forces between junctions were thus proposed to be the main cause of friction. However, apart from adhesion, a *plowing* effect was found to be important for rougher surfaces , in which a harder material penetrates the softer, producing grooves - the energy required for their creation must be supplied by the friction.

Remarkable velocity- and slip- dependent departures from Coulomb's model of friction were first documented by Rabinowicz (1951) and, following the suggestion by Brace and Byerlee (1966), that friction plays an important role in the process of earthquake nucleation, later rediscovered in experiments by Ruina, Dieterich, Scholz and others. It was found that the coefficient of static friction increases with time and that kinetic friction exhibits nontrivial velocity and time dependence. The *rate-and-state* laws of friction were developed at the late seventies and early eighties as a constitutive macroscopic framework to phenomenologically incorporate the understanding of friction gained from the laboratory experiments. A great deal of work was done in which the rate-and-state friction was applied in modeling the behavior of seismic faults. The laws have been successful in reproducing "virtually the entire range of observed seismic and interseismic fault behaviors, ranging from preseismic slip and earthquake nucleation...to coseismic rupture... and earthquake afterslip.... In addition, the laws have been widely used to describe systematic variations in seismic behavior, including the depth of seismic faulting, variation of stress drop with earthquake recurrence interval ...seismic slip complexity...variations in the stability and seismic coupling at subduction zones...and characteristics of aftershock decay" (Marone, 1988). Below, we provide a very brief overview of of aforementioned friction experiments, formulate the rate-and-state laws and show how they can be used to match the experimental results.

1.3 Rock friction experiments

It is not our aim to give an extensive and detailed account of the experiments on rock friction. Instead, we concentrate schematically on two basic types of experiments that capture the most important effects that led to the formulation of RS laws. These are the velocity-step and slide-hold-slide experiments. We will mention some important corrections stemming from other experiments later.

In both of the experiments two rocks of apparently planar contact interfaces are compressed by a constant effective normal stress $\bar{\sigma}$ and forced to slide over each other by some loading of high effective stiffness k (i.e. it is assumed that the elastic coupling of the materials to external loading can be modeled with a spring). The effective normal stress is defined to account for the effect of possible fluid permeation of rocks by the relation

$$\bar{\sigma} = \sigma - p, \tag{1.2}$$

where $\sigma$is the confining normal stress and p is the pore pressure exerted by the fluid. The movement of the rocks is confined so as to have only one degree of freedom perpendicular to the direction of normal stress. The relative motion of rocks is called *slip* and we will denote it by δ. The time-derivative of slip is called *slip velocity* or *slip rate* and we will denote it by the letter V. The slip rate in the experiments is typically low, of the order $0.01 - 1000\ \mu m/s$. In all the experiments, the shearing stress τ acting on the interface plane - *friction* is measured at all times. The coefficient of friction μ is defined as

$$\mu = \frac{\tau}{\bar{\sigma}} \tag{1.3}$$

In the velocity-step experiment the rocks are first forced to slide at constant velocity V_1. After some time, a steady-state sliding is observed, in which the friction settles to a constant value τ_1. Then a sudden jump to a new velocity V_2 is enforced by the loading. The graph of friction against slip is shown on figure 1.1. The most important features of observed frictional behavior are as follows:

1. Right after the velocity jump, there is an instantaneous change in friction with the same sign as the change of velocity. It was found that the change of friction due to the velocity jump $\Delta\tau(V_1 \to V_2)$ is approximately proportional to the logarithm of the ratio between the two velocities: $\Delta\tau(V_1 \to V_2) = A \ln \frac{V_2}{V_1}$. The constant of proportionality is $A = a\bar{\sigma}$, where a is a parameter that depends on both the material used and external conditions. The typical order of a is about $10^{-2} - 10^{-1}$. This came to be called the *direct (velocity) effect.*

2. After the jump, there is an approximately exponential relaxation towards a new steady-state value of friction, which depends solely on the new velocity (in the sense that it does not depend on the history of sliding). The slip distance over which this relaxation happens is called the *characteristic* or *critical slip distance* and is denoted by D_C or L in the literature (in this thesis, we use D_C). The relaxation curve to the steady-state is symmetric for jumps of opposing logarithmic magnitude. in figure 1.1, we can see that the new steady-state value is smaller than the original one. Since $V_2 > V_1$ in this case, this means that the steady-state value of friction decreases with velocity. Accordingly, this behavior is called *velocity-weakening.* For some conditions and materials, particularly for lower values of normal

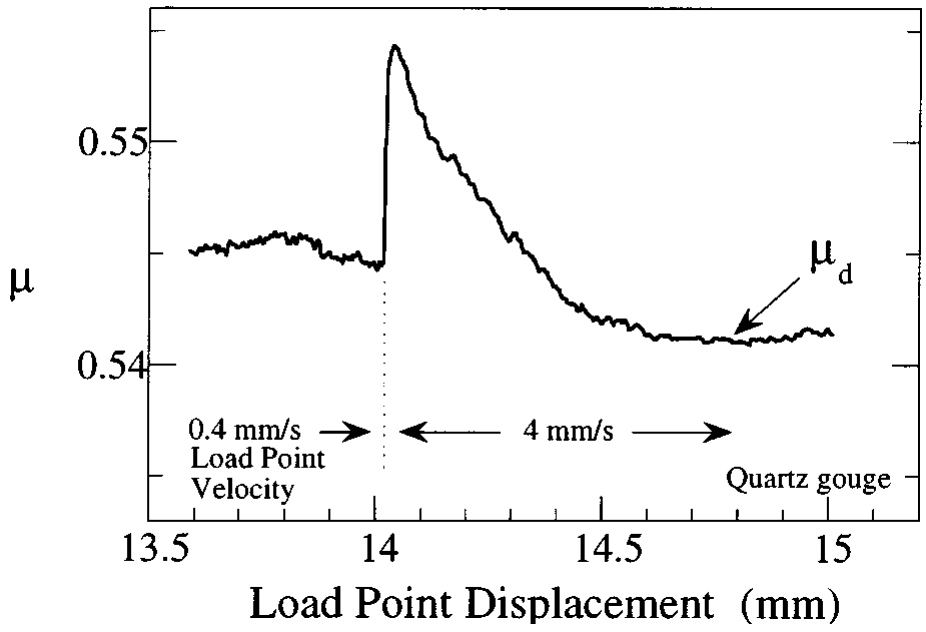

Figure 1.1: Friction vs slip in the velocity step test. After Marone (1998)

stress and higher temperatures, the opposite behavior - called *velocity-strengthening* - is observed. The dependence of steady-state friction τ_{SS} on velocity was found to follow

$$\tau_{SS}(V) = const + c\bar{\sigma} \ln V, \tag{1.4}$$

where c is a parameter that can be both positive and negative (corresponding to the velocity-strengthening and velocity-weakening behavior, respectively).

The velocity-step experiment shows that the coefficient of friction is a function of velocity. However, it is clear that it cannot be a single valued function of velocity, as there is a time/slip dependence of friction during it's relaxation to the steady-state value. In other words, there is an evolutionary effect dependent on the history of slip.

The slide-hold-slide tests show another type of time dependence of friction. In this experiment, the rock is again at first loaded with constant velocity. The load is then stopped for some time Δt and released again. The corresponding change in friction can be seen on figure 1.2. As we can see, first there is a rapid decrease in the friction coefficient (this can be interpreted to be a result of the direct velocity effect) and then a rapid increase. The local maximum of friction is interpreted as a new value of *static friction* μ_S. As we can see from figure 1.2, static friction is increasing with the hold time. This phenomenon has

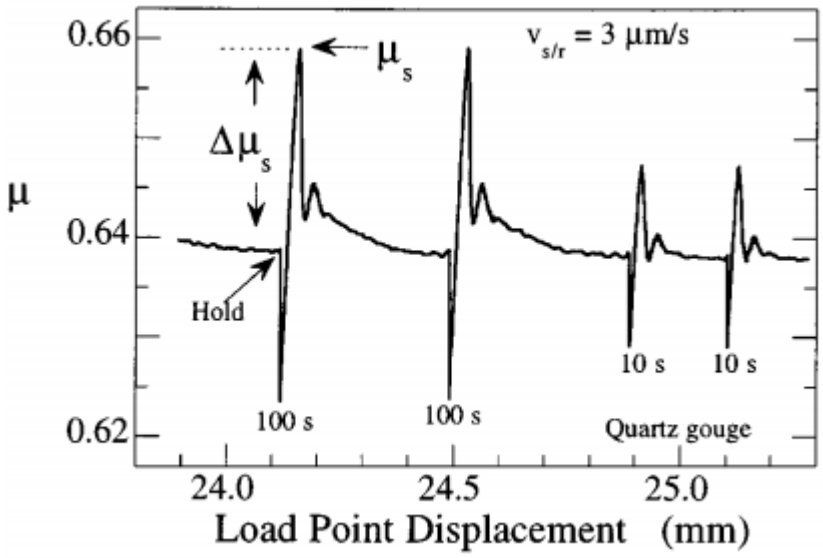

Figure 1.2: Friction vs slip in the slide-hold-slide test. After Marone (1998).

been called *healing, aging* or *strength recovery.* Note that simple friction laws dependent only on slip or velocity are incapable of describing this phenomenon.

It was found that the dependence of healing on the hold time can be described by the relation (Paterson, 2005):

$$\mu_S = \mu_{S_0} + \beta \ln(1 + \frac{\Delta t}{t_C}), \tag{1.5}$$

where μ_{S0}, β and t_C are constants.

Figure 1.3 shows the dependence of static friction on the hold time in logarithmic scale as measured by several authors.

Finally, we note that a general feature of sliding experiments is that the rocks can exhibit both stable sliding as well as unstable, stick-slip behavior. The regime of stability depends not only on the materials, but also on the experimental apparatus- transition from stable to unstable regime can be induced by decreasing the load stiffness or by increasing the effective pressure or the loading velocity (Dieterich, 1979).

1.4 Formulation of the rate-and-state laws

As we have seen, a macroscopic constitutive law for friction should be able to incorporate a direct velocity-dependent effect as well as evolutionary effects - relaxation and healing. The rate-and-state framework accounts for the evolutionary effects by assuming that they happen due to evolution of an interfacial

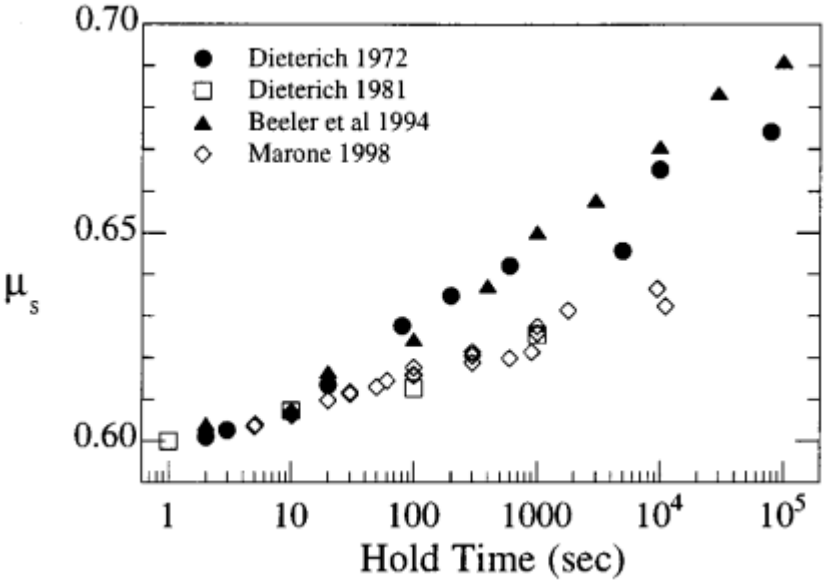

Figure 1.3: Dependence of static friction on hold time. Logarithmic scale for the hold time is used. After Marone (1998)

state. This state is determined by a finite number of values of *state variables* θ_i,. For simplicity, only one state variable θ is usually considered, for the price of a possibly worse fit of the RS laws to experiments. Most of the rate-and-state modeling was done with one state variable. Rate-and-state laws are defined by the constitutive law

$$\tau(V(t),\theta(t)) = F(V(t),\theta(t)) = \bar{\sigma}(t)\left(\mu_* + a\ln\frac{V(t)}{V_*} + b\ln\frac{V_*\theta(t)}{D_C}\right), \qquad (1.6)$$

where μ_*, V_*, a, b and D_C are all positive parameters and the *evolution law*, which is a first order differential equation for θ:

$$\frac{d\theta}{dt} = G(V,\theta), \qquad (1.7)$$

with some function $G(V,\theta)$. The evolution law tries to capture the essential dynamics of the interfacial state. The form of F as given in eq. (1.6), called the *Dieterich-Ruina* constitutive law, is almost exclusively used in modeling (apart from possible regularization). However, several forms for G have been proposed.

The most common forms of G are the *ageing law:*

$$\frac{d\theta}{dt} = G_{aging}(V,\theta) = 1 - \frac{V\theta}{D_C} \qquad (1.8)$$

and the *slip law*:

$$\frac{d\theta}{dt} = G_{slip}(V,\theta) = -\frac{V\theta}{D_C}\ln\frac{V\theta}{D_C} \tag{1.9}$$

Both laws capture the essential features of experiments, but differ in their ability to explain specific details.

Let us show that the equation (1.6) coupled with equation (1.8) is able to reproduce the described features obtained from experiments.

First, let's solve for the steady-state in which $d\tau/dt = 0$. Like in the experiments, let us suppose that both $\bar{\sigma}$and V are fixed. The condition for steady state then reduces to

$$\frac{d\theta}{dt} = G\left(\theta(t), V(t)\right) = 0, \tag{1.10}$$

which implies

$$\theta_{SS}(V) = \frac{D_C}{V}, \tag{1.11}$$

where we have used the subscript $_{SS}$ for steady-state (this is true regardless of the evolution law G used). Plugging this into eq. (1.6) we obtain

$$\tau_{SS}(V) = \bar{\sigma}\mu_* + \bar{\sigma}(a-b)\ln\frac{V}{V_*}. \tag{1.12}$$

Comparing this to eq. (1.4) we see that the constant of proportionality c corresponds to the value of $a-b$ in the rate-and-state formalism. Thus, for $a > b$ we have velocity strengthening, and for $a < b$ we have velocity weakening. In general, larger values of $\bar{\sigma}a$ promote stability and larger values of $\bar{\sigma}b$ promote unstable behavior (this will be seen in more detail in the following section). From this formula, it is clear that the meaning of μ_* is simply the friction coefficient for steady-sliding at referential velocity V_*.

Next, let us show the effect of direct velocity step change. Let assume that the rock is sliding in steady-state with velocity V_1 and let it suddenly change to V_2 at time $t = 0$. Before the step change, friction is given by the steady state formula above

$$\tau(0^-) = \tau_{SS}(V_1) = \bar{\sigma}\mu_* + \bar{\sigma}(a-b)\ln\frac{V_1}{V_*} \tag{1.13}$$

After the step change, θ will not have changed, because its evolution is given by a solution of the differential equation (1.7) (we assume it is continuous), so it's value will be $\theta(0) = \frac{D_C}{V_1}$. Inserting this value into (1.6) we see that the value of τ right after the velocity jump will be

$$\tau(0^+) = \bar{\sigma}\left(\mu_* + a\ln\frac{V_2}{V_*} + b\ln\frac{V_*}{V_1}\right) = \bar{\sigma}\left(\mu_* + a\ln\frac{V_2}{V_1} + (a-b)\ln\frac{V_1}{V_*}\right). \tag{1.14}$$

Thus, for the jump in friction, we have:

$$\Delta\tau(V_1 \to V_2) = \tau(0^+) - \tau(0^-) = \bar{\sigma}a\ln\frac{V_2}{V_1}, \tag{1.15}$$

which is in agreement with the observations from velocity-step experiments. Therefore, the second term represents the magnitude of the direct velocity effect as anticipated. Again, this holds regardless of the evolution law used.

Next, let's see how the rate-and-state law accounts for the exponential relaxation after velocity jump. Let us use the aging law (1.8). Since after the jump, velocity is kept fixed at value V_2, the differential equation (1.8) is easily solved for $\theta(t)$:

$$\theta(t) = (\theta_0 - \frac{D_C}{V_2}) \exp(-\frac{V}{D_C}t) + \frac{D_C}{V_2}. \tag{1.16}$$

Noting that we again have $\theta_0 = \frac{D_C}{V_1}$ and plugging the above equation into (1.6) we get

$$\tau(t) = \bar{\sigma} \left[\mu_* + (a-b) \ln \frac{V_2}{V_*} + b \ln \left(1 + (\frac{V_2}{V_1} - 1) \exp(-\frac{V_2}{D_C}t) \right) \right]. \tag{1.17}$$

From the Taylor expansion of logarithm, we can see that for larger values of t this indeed gives an approximate exponential decay with characteristic slip distance D_C to the steady-state value $\tau_{SS}(V_2)$. On the other hand, for small t this approximation will not hold, so the "relaxation" time will depend on the initial conditions, which would not be the case for a purely exponential decay. Also, the relaxations following a logarithmic jump of same amplitudes but different sign (i.e. $|\ln V_2 - \ln V_1| = const$) are not symmetric for the ageing law. If had used the evolution law (1.9) instead, then the relaxation would have been both exponential and symmetric.

Finally, let's take a look at time-dependent healing. Again, let us suppose that the rock first slides in steady state with velocity V_1, so the friction is given by (1.13). Velocity is then forced go to very small values for a duration of Δt, before returning back to V_1. During the low velocity phase, we have $V \ll \frac{D_C}{\theta}$. Then the second term in the evolution law (1.8) may be neglected:

$$\frac{d\theta}{dt} = 1, \tag{1.18}$$

so θ can simply be interpreted as the hold time, $\theta(t) = \theta(0) + t$ (this is the origin of the name *ageing law*), during this phase. Realizing that $\theta(0) = \theta_{SS}(V_1) = \frac{D_C}{V_1}$, we see that right after releasing at $t = \Delta t$, θ will have the value of $\frac{D_C}{V_1} + \Delta t$. Plugging into the constitutive law, we get

$$\begin{aligned} \tau(\Delta t) = \bar{\sigma} \left(\mu_* + a \ln \frac{V_1}{V_*} + b \ln \left[\frac{V_*}{V_1} (1 + \frac{V_1 \Delta t}{D_C}) \right] \right) = \\ = \bar{\sigma} \left(\mu_* + (a-b) \ln \frac{V_1}{V_*} + b \ln \left[1 + \frac{V_1 \Delta t}{D_C} \right] \right). \end{aligned} \tag{1.19}$$

Subtracting the steady state friction before hold, we find that

$$\Delta \tau_{hold} = \bar{\sigma} b \ln(1 + \frac{V_1 \Delta t}{D_C}). \tag{1.20}$$

Comparing this to the empirical relation for healing (1.5), we see that two expressions match if we identify $\beta = \bar{\sigma} b$. If we had used the evolution law *(1.9)* instead, we would not be able to obtain the result this way, because in that case $d\theta/dt \to 0$ for $V \to 0$ (hence the name *slip law*). However, it is still possible to obtain healing when the effect of coupling to external loading is included, in which case the rock still undergoes non-zero slip even while the loading is being held (since the stiffness is finitely small). Nevertheless, experiments by Beeler et al. (1994) and Nakatani and Mochizuki (1996) with loadings of different stiffness showed that healing is a function of time, not slip, so (1.9) does not provide an adequate description of healing.

To summarize, we have shown that the rate-and-state laws are capable of reproducing the observations seen in velocity-step experiment and the healing effect of the slide-hold-slide experiment. The first term of the constitutive law (1.6) represents steady-state friction at a referential velocity V_*. The second term, which is proportional to a dimensionless parameter a represents the direct velocity effect. The third term, proportional to parameter b represents an evolution effect, which accounts for both healing and relaxation. The relaxation occurs over a critical distance D_C. The aging law better explains the time-dependent healing, while the slip law more accurately describes the exponential relaxation to steady-state.

Let us add a few remarks:

- One might be concerned with the fact that the constitutive law (1.6) implies negative values of τ for V small enough and that for $V = 0$ it is even undefined. To avoid this, the expression can be regularized around $V = 0$ to

$$\tau(V(t), \theta(t)) = \bar{\sigma}(t) \left(\mu_* + a \ln(1 + \frac{V(t)}{V_*}) + b \ln(1 + \frac{V_* \theta(t)}{D_C}) \right) a, \quad (1.21)$$

  which agrees with (1.6) for $V/V_* \gg 1$, $V_*\theta/D_C \gg 1$. Another way to regularize the constitutive law is (Lapusta, 2012):

$$\tau(V(t), \theta(t)) = a\bar{\sigma} \sinh^{-1} \left[\frac{V}{2V_*} \exp\left(\frac{\mu_* + b \ln(V_*\theta/D_C)}{a} \right) \right] \quad (1.22)$$

  which again agrees with (1.6), because $\sinh^{-1}(x)$ can be approximated as $\ln(2x)$ for larger values of x. This form is actually suggested by physical explanations for rate-and-state friction (Putelat, 2011). We touch on this subject in the next section.

- It is possible to use different quantities for the state variable. For example, if instead of θwe use Θ defined as

$$\Theta = b \ln \frac{V_* \theta}{D_C} \quad (1.23)$$

  then we get in place of the constitutive law(1.6):

$$\tau(V(t), \Theta(t)) = \bar{\sigma}(t) \left(\mu_* + a \ln \frac{V(t)}{V_*} + \Theta(t) \right) \quad (1.24)$$

and

$$\frac{d\Theta}{dt} = \frac{bV_*}{D_C}\left[\exp\left(-\frac{\Theta}{b}\right) - \frac{V}{V_*}\right] \tag{1.25}$$

in place of the ageing law (1.8). Note that the velocity and the state variable are separated in this form of ageing law. Based on this form, Nakatani (2001) offers a slightly different point of view of the rate-and-state laws. He notes that if we invert (1.24) for velocity, then we obtain

$$V(\tau, \Theta) = V_* exp\left(\frac{\tau/\sigma - (\mu_* + \Theta)}{a}\right). \tag{1.26}$$

Looking through the prism of this formula, we can view the velocity as a response (output) to the applied stress (input). The term $\mu_* + \Theta$ can be interpreted as the interfacial *strength,* which evolves in accordance with equation 1.25. This connects the rate-and-state laws with the classical understanding of friction, in which both static and a dynamic friction can be understood as a threshold force required for an object to start moving (in the case of static friction) or keep moving (in the case of dynamic friction). This is because once the value of τ/σ falls below $\mu_* + \Theta$, the argument in exponential will be negative and since a is of the order of $10^{-2} - 10^{-1}$, V will be close to zero. We also see that it's possible, in principle, to measure $\mu_* + \Theta$ by rapidly imposing a sliding velocity V_* and measuring the stress τ required to do it.

- Since neither the aging law nor the slip law are able to describe exactly the entire range of behavior seen in experiments, a number of alternate evolution laws have been proposed. Let us mention but a few examples. The PRZ law (from Perrin, Rice and Zhenga)

$$\frac{d\theta}{dt} = 1 - \left(\frac{V\theta}{D_C}\right)^2 \tag{1.27}$$

accounts for the asymmetrical relaxation towards steady-state by squaring the second term in the ageing law. However, this makes the relaxation too rapid. The composite law

$$\frac{d\theta}{dt} = \exp\left(-\frac{V}{V_C}\right) - \frac{V\theta}{D_C}\ln\frac{V\theta}{D_C} \tag{1.28}$$

combines the time dependent healing of the aging law at small velocities and behaves like the slip law for $V \gg V_C$. Nagata et al. (2012) proposed adding a term proportional to $d\tau/dt$ to the evolution law (1.25)

$$\frac{d\Theta}{dt} = \frac{bV_*}{D_C}\left[\exp\left(-\frac{\Theta}{b}\right) - \frac{V}{V_*}\right] - c\frac{d\tau}{dt} \tag{1.29}$$

for some parameter c. Nagata suggested that this law could remedy the problems in both the ageing and the slip law. However, this was recently questioned by Bhattacharya et al. (2013).

- The rate-and-state law (1.6) and (1.8) laws are able to model the most commonly observed experimental features under constrained experimental conditions we described. However, in more general settings, the rate-and-state laws can be extended to account for a various number of effects. This can be done by adding additional terms into the evolution law or by slightly modifying the constitutive law. Relevant to us is the result of Linker and Dieterich (1992), who showed that in the presence of variable normal stress, the ageing law has to be modified to

$$\frac{d\theta}{dt} = 1 - \frac{V\theta}{D_C} - \frac{\alpha}{b}\frac{\dot{\sigma}}{\sigma}\theta, \tag{1.30}$$

where α is a constant estimated to have a value around $\mu_*/3$. For $\mu_* = 0.6$, we can take $\alpha = 0.2$. This form of law will be used to model reactions to external applications of stress. Other phenomenons that the rate-and-state laws can be corrected for include the effect of shear dilatancy, flash heating, melting, pore-pressure evolution, slip, etc. (Lapusta, 2012).

1.5 A physical basis for rate and state laws

It may seem that the rate-and-state laws, despite their success at capturing the essential features of friction seen at experiments are somewhat arbitrary and lack a satisfactory micro-physical explanation. Indeed, a complete account of friction from first principles is still missing. Nevertheless, theories that provide some physical insight into the mechanism of rate-and-state friction were proposed. An interesting discussion of these was given by Putelat (2011), here we reiterate some of his arguments.

At the beginning of this chapter we mentioned that two materials in contact do not touch over their whole apparent area of contact A, but interact at only a small number of asperities, whose real contact area is A_r. Let us By the assumption of Bowden and Tabor, both the macroscopic normal force N and the friction force F are proportional to the real contact area A_r:

$$N = A_r\sigma_c, \qquad F = A_r\tau_c, \tag{1.31}$$

with σ_c and τ_c denoting the stresses at asperity junctions. For the coefficient of friction μ, this implies

$$\mu = \frac{F}{N} = \frac{\sigma}{\tau} = \frac{\tau_c}{\sigma_c}, \tag{1.32}$$

where $\sigma$and $\tau$are the macroscopic normal and shear stresses (Note that Berman et al. (1998) show that the assumptions (1.31) do not always hold and that the concept of contact area on molecular level may not even be a meaningful concept. They conclude that the proportionality of frictional force to normal force is obeyed directly at molecular level and so the Bowden and Tabor postulates (1.31) may not be needed).

Two possible explanations for the origin of the constitutive friction law (1.6) are presented: a constitutive theory resting on the assumptions (1.31) and a thermodynamic theory, which makes direct use of eq. (1.32). Both of these explanations are based on the transition rate theory, which gives a frequency $v$with which an event occurs if it has to overcome an energy barrier E_*:

$$v = v_0 \exp(-\frac{E_*}{k_B T}), \tag{1.33}$$

where v_0 is a reference velocity, T the temperature and k_B the Boltzmann constant. In the presence of deformation Σ acting on an activation volume Ω, the frequency changes to

$$v^{\pm} = v_0 \exp(-\frac{E_* \mp \Sigma\Omega}{k_B T}), \tag{1.34}$$

where the sign depends on whether the transition goes in the forward direction $(-)$ or the backward direction $(+)$. The constitutive theory assumes a decomposition of the friction force in a form $F(\theta, V) = A_r(\theta)\tau_C(V)$, i.e. the real contact area depends only on the state variable and the yield stress only on velocity. It then invokes constitutive laws involving eq. (1.34) and Nabarro–Herring creep for each part of the decomposition, which allows to obtain Dieterich-Ruina's law after linearization. The thermodynamic theory directly applies eq. (1.34) to obtain a frequency $v^{\pm}$ with which a slip patch overcomes an energy barrier of asperities E_* in an activation volume $\Omega = \Omega_*$, while shearing them at constant stress $\Sigma{=}\tau_c$. The activation volume Ω_* is defined as $\Omega_* = E_*/\tau_Y$, where τ_Y is the yield stress of asperity junction - i.e. it is assumed that asperities undergo shear once the local stress reaches the yield stress value. Assuming that with each successful slip event, the patch moves an average distance λ, we obtain an expression for the velocity V

$$V = \lambda(v^+ - v^-) = 2\lambda v_0 \exp\left(-\frac{E_*}{k_B T}\right) \sinh\left(\frac{\tau_c \Omega_*}{k_B T}\right). \tag{1.35}$$

Using the eq. (1.32) and defining $a = k_B T/(\Omega_* \sigma_c)$ and $V_* = \lambda v_0$, this can be rewritten as

$$V = 2V_* \exp\left(-\frac{E_*}{k_B T}\right) \sinh\left(\frac{\tau}{a\sigma}\right). \tag{1.36}$$

Inverting this expression for τ, we get

$$\tau = a\sigma(t) \sinh^{-1}\left[\frac{V}{2V_*} exp\left(\frac{E_*}{k_B T}\right)\right], \tag{1.37}$$

The velocity dependence here is exactly the same as that in the regularized version of the RS law (1.22). Comparing the two formulas, we see that to match, we need to have

$$E_* = \Omega_* \sigma_c(\mu_* + bln\frac{\theta}{\theta_*}) \tag{1.38}$$

and since $E_* = \Omega_* \tau_y$, we obtain an expression that relates the state variable to the asperity yield stress τ_Y

$$\tau_Y = \sigma_c(\mu_* + b \ln \frac{\theta}{\theta_*}). \tag{1.39}$$

Actually, if we used the state variable Θdefined by (1.23), this would read

$$\tau_Y = \sigma_c \Theta \tag{1.40}$$

which suggests that the state variable Θ is directly proportional to the evolution of asperity yield stress. The aging law would then correspond to a logarithmic increase of yield stress with contact time.

1.6 Stick slip and the spring slider

Stick-slip is a repeating jerking motion composed of two phases - *stick,* in which an object is at rest (or moves with negligible velocity) and accumulates potential energy, and *slip,* during which this energy is converted into kinetic energy with sudden acceleration. This motion is a result of the non-linear dynamics of friction and apart from acting as a mechanism of earthquakes, it may be encountered in a wide range of situations such as landslide motions, creaking of a slowly opened door, screeching of chalks moving on blackboards, the sound of a bow moving over the strings of a violin or a cello, a grasshopper rubbing its legs together, fingers moving along the edge of dry glass, the sound of heavy braking of a car or train or many other engineering contexts (di Liberto, 2015).

In this section, we explain the phenomenon of stick-slip by using a simple spring-slider model, which is relevant to our modeling. To elucidate some of its basic features, we use the Coulomb model of friction which immediately enables us to solve the equation of motion. Then we show a standard linearized stability analysis for the rate-and-state friction.

1.7 Spring Slider

The spring slider is simply a body (block) of mass M sliding on a planar surface (floor) with friction force F_f and connected to a spring of stiffness k whose fixed end moves with a constant velocity. Here, we choose to work in an inertial frame in which the fixed end is at rest and the *loading* velocity of the underlying plate is v_{pl}. This shown in fig. 1.4. We denote the position of the slider in this frame by x.

The position of the center of mass of the slider satisfies the equation

$$M\ddot{x} + k(x - x_0) - F_f(\dot{x} - v_{pl}, \cdots) = 0, \tag{1.41}$$

where x_0 is the equilibrium position of the spring. We choose $x_0 = 0$. In the arguments of frictional force, we explicitly denote the dependence on relative

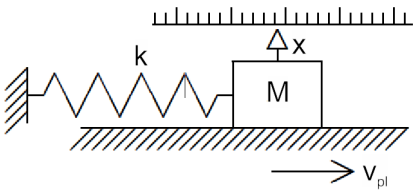

Figure 1.4: A spring slider model in the rest frame of the fixed end of the spring. Taken after Elmer (1997).

velocity $v_{rel} = \dot{x} - v_{pl}$, while the dots represent any other general parameter that F_f might depend on. Here we use the Coulomb's model of friction $F_f = F_C$, where $F_C \leq \mu_s N$ for $v_{rel} = 0$ and $F_C = \mu_k N sign(v_{rel})$ for $\dot{x} < v_{pl}$, where N is the normal force acting on the block. The coefficients μ_s and μ_d, $\mu_s > \mu_d$ are called the *static* and *kinetic* coefficients of friction, respectively. The inequality $F_C \leq \mu_S N$ for $v_{rel} = 0$ means that the friction will exactly match any force smaller than $\mu_S N$. Thus, for $\dot{x} = v_{pl}$ and $kx < \mu_s N$, the last two terms on the LHS of equation (1.41) cancel and it simplifies to

$$M\ddot{x} = 0. \tag{1.42}$$

For $\dot{x} = v_{pl}$ and $kx = \mu_s N$ or for $\dot{x} < v_{pl}$ the equation goes to

$$M\ddot{x} + kx + \mu_k N sign(\dot{x} - v_{pl}) = 0. \tag{1.43}$$

1.8 Solution of the equations of motion

Let the block initially slide with the surface, i.e. $\dot{x}(t_0) = v_{pl}$ and let it's initial position be zero, $x(t_0) = 0$. Static friction and eq. (1.42) will then apply and the friction force will exactly balance the force exerted by the spring, $F_C = kx$. The block will slide with velocity $\dot{x} = v_{pl}$ and its position will increase linearly with time $x = vt$. However, once the spring force reaches the threshold value, $kx = \mu_s N$, static friction will change to dynamic and eq. (1.43) will start to apply with initial conditions $x(t_1) = \frac{\mu_s N}{k}$ and $\dot{x}(t_1) = v$, where $t_1 = \frac{\mu_s N}{kv}$. It has the solution

$$x(t) = \frac{\mu_k N}{k} + \frac{\mu_s - \mu_k}{k} N \cos\left(\omega(t - t_1)\right) + \frac{v_{pl}}{\omega} \sin\left(\omega(t - t_1)\right), \tag{1.44}$$

where $\omega = \sqrt{\frac{k}{M}}$. This solution describes the slip phase of the cycle. It will be valid until some time t_2, for which $v_{rel}(t_2) = 0$. At that point, the friction will change back from dynamic to static and eq. (1.42) will start to apply once again - the block will get locked with the floor until the spring force once again

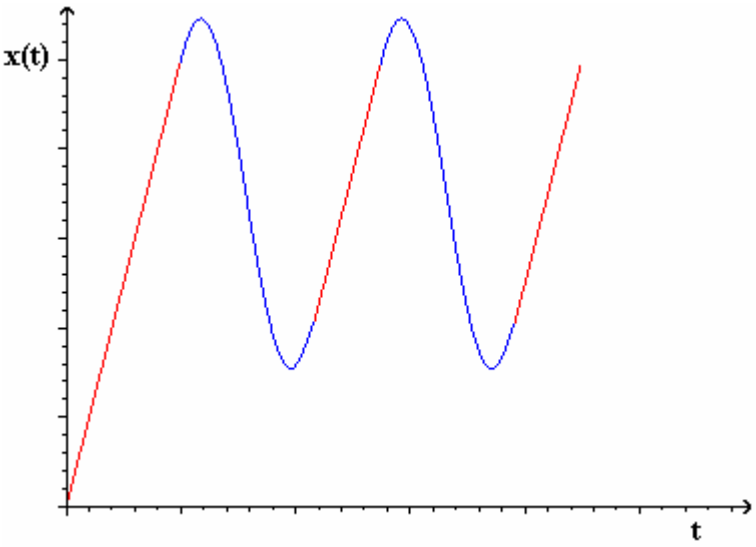

Figure 1.5: Stick slip of the slider as seen in the reference frame co-moving with the spring's fixed end . The red parts of the curve represent the *stick*, blue parts *slip*. After Liberto *(*2015*)*.

reaches the threshold value. This is the stick phase of the cycle. This *stick-slip* behavior will continue indefinitely. We show this on figure 1.5.

Let us now examine the durations T_{slip} and T_{stick} of the slip and stick phase respectively. The phases are delineated by times t_i for which $v_{rel}(t_i) = 0 \Leftrightarrow \dot{x}(t_i) = v_{pl}$. In the slip phase, motion is given by the equation 1.44. This is a sum of two harmonic functions (plus the offset $\frac{\mu_k N}{k}$) which can always be represented as a single cosine function of amplitude A and phase $\phi = \arctan(\frac{v/\omega}{\frac{\mu_S - \mu_k}{k}})$:

$$x(t) = \frac{\mu_k N}{k} + Acos(\omega t + \phi). \tag{1.45}$$

The duration of the slip will depend on this phase. For v_{pl} relatively small, $\frac{v_{pl}}{\omega} < \frac{\mu_s - \mu_k}{k} N$, the sine term can be neglected and $\phi = 0$. The slip phase will then be equal to the half period, $T_{slip} = \frac{T}{2} = \frac{\pi}{\omega}$. For increasing v_{pl} or k, the phase will also increase, as well as the time interval between events for which $\dot{x} = v_{pl}$, i.e. T_{slip} is going to increase, with an asymptotic value of Tas $\phi \to \frac{\pi}{2}$. During the stick, the slider moves with a velocity of v over the distance $2\frac{\mu_S - \mu_D}{k} N$ (this is the distance between the two closest positions for which $\dot{x} = v_{pl}$). We thus must have $T_{stick} = 2\frac{\mu_s - \mu_D}{kv} N$. As we can see, the duration of the slip phase increases with v_{pl} and k and it decreases with the difference between static and dynamic friction, $\mu_S - \mu_D$. The duration of the stick phase on the other hand goes to zero when the product of kv_{pl} is significantly larger than $(\mu_s - \mu_D)N$. Thus, for a given material, the stick phase of the slip can be minimized by

increasing the velocity or stiffness of the load. This effect is commonly observed in squeaky doors - their squeaking can be reduced by opening them fast.

If we had used different initial conditions for which $\dot{x}$ never exceeded v_{pl}, then the block would behave as an undamped harmonic oscillator - we wold get continuous, uninterrupted sliding. Thus, in the Coulomb friction model, both continuous sliding and stick-slip behavior can exist - depending on initial conditions - for every configuration of parameters. There is no critical threshold below which there's stick slip and above which there is not. For more general models of velocity dependent friction, this coexistence of regimes exists for only a limited range of parameters - for example, there always exists a critical loading velocity above which no stick-slip can exist (Elmer, 1997). In the model of spring slider with rate-and-state friction, there is a bifurcation in critical stiffness at which steady-sliding becomes impossible. We show this in the next section.

1.9 Linear analysis of stability of rate-and-state system

Here we show a linear analysis of the spring-slider system with rate and state friction. The results of this analysis were given by Rice (1983), we use a less elegant, but more simple derivation here.´To make the presentation more lucid, we use a general form of constitutive and evolution laws depending on the slip rate $V = \frac{dx}{dt}$ and the state variable θ, $\tau_{fr} = F(\theta, V)$ and $\dot{\theta} = G(\theta, V)$, respectively. Without loss of generality we also assume that the slider has unit area, so that $\tau_{el} = F_{el}$ and $\tau_{fr} = F_{fr}$. For this analysis, it is easier to go to a frame in which the floor is stationary and the fixed end of the spring moves with velocity V_{pl}. The system is then defined by equations

$$M\frac{d^2x}{dt^2}(t) + \tau_{el}(t) - \tau_{fr}(t) = 0, \tag{1.46}$$

where

$$\tau_{el}(t) = k(V_{pl}t - x(t)), \tag{1.47}$$

$$\tau_{fr}(t) = F(V(t), \theta(t)) \tag{1.48}$$

and

$$\frac{d\theta(t)}{dt} = G(V(t), \theta(t)). \tag{1.49}$$

We shall linearize this system around the state of steady-sliding at velocity V_{pl}, at which $V = V_{pl}$ and $\tau_{fr}(V, \theta) = \tau_{SS}(V_{pl})$, where τ_{SS} is the value of steady-sliding friction at V_{pl}. Let us denote the values of all quantities at the steady-sliding state with the subscript $_{SS}$ and define increments: $x'(t) = x(t) - x_{SS}(t)$, $V'(t) = V(t) - V_{SS}, \tau'(t) = \tau'(t) - \tau(V_{SS}), \theta'(t) = \theta(t) - \theta_{SS}(V_{SS})$. Note that $V_{SS} = V_{pl}$ and $x_{SS}(t) = V_{pl}t$. After the linearization, we obtain a set of equations for these increments:

$$M\frac{d^2x'}{dt^2} + \tau'_{el} - \tau'_{fr} = 0, \tag{1.50}$$

$$\tau'_{el} = -kx', \tag{1.51}$$

$$\tau'_{fr} = F_V V' + F_\theta \theta' \tag{1.52}$$

and

$$\frac{d\theta'}{dt} = G_V V' + G_\theta \theta', \tag{1.53}$$

where the subscripts at F and G denote partial derivatives evaluated at the steady state. Differentiating eq. (1.50), (1.51) and (1.52) with respect to time and using the equation (1.53), , we obtain after a simple algebra a linear differential equation in x':

$$-M\frac{d^3x'}{dt^3} + (F_V + G_\theta M)\frac{d^2x'}{dt} + (k - G_\theta F_V + F_\theta G_V)\frac{dx'}{dt} - G_\theta k x' = 0. \tag{1.54}$$

Assuming a solution of the form

$$x'(t) = Ae^{st},\ s \in \mathbb{C} \tag{1.55}$$

we get a cubic equation for s:

$$-Ms^3 + (F_V + G_\theta M)s^2 + (k - G_\theta F_V + F_\theta G_V)s - G_\theta k = 0. \tag{1.56}$$

If $\mathrm{Re}(s) < 0$ then any perturbation from the steady state will decay exponentially. On the other hand, if $\Re e(s) > 0$ then steady-state sliding cannot exist, since any small perturbation will grow exponentially. Let us find the critical stiffness k_{crit}, for which $\mathrm{Re}(s) = 0$. First, let's assume the limit in which inertia can be neglected, $M = 0$, which is the limit we use in our modeling. In literature, this case is referred to as the *quasi-static* regime. Equation (1.56) will then reduce to

$$(F_V)s^2 + (k - G_\theta F_V + F_\theta G_V)s - G_\theta k = 0. \tag{1.57}$$

This is a quadratic equation for s, whose solutions are:

$$s = \frac{1}{2F_V}\left[-D \pm \sqrt{D^2 + 4F_V G_\theta k}\right], \tag{1.58}$$

where

$$D = k - (G_\theta F_V - F_\theta G_V) \tag{1.59}$$

Assuming that $F_V > 0$ and $G_\theta < 0$ (as is the case for rate-and-state friction) we see that the real part of the square root is necessarily smaller than D. Thus, $\mathrm{Re}(s) < 0$ if and only if $D > 0$. From (1.59) we see that this happens for values of k such that

$$k > k^0_{crit} = G_\theta F_V - F_\theta G_V \tag{1.60}$$

and $\mathrm{Re}(s) > 0$ for $k < k^0_{crit}$. Since the loss of stability occurs when s crosses the imaginary axis, we speak of Hopf bifurcation at $k = k^0_{crit}$. Note that if the product $F_V G_\theta$ were positive, then the square root in (1.58) would be positive. Consequently, we'd always have $Re(s) > 0$ for one of the solutions. Since the

positivity of the direct velocity effect, $F_V > 0$ as well established from laboratory experiments, this means that $G_\theta < 0$ is a necessary constraint on the evolution law for stable solutions to exist in the quasi-static regime.

For completeness, let us give the formula for critical stiffness in presence of mass, $M \neq 0$. This could in principle be found by solving the cubic equation (1.56) or utilizing a Laplace transform as in Rice (1983). Here, we instead note that since the left hand side of (1.56) is linear in both k and M, k_{crit} is a linear function of M:

$$k_{crit}(M) = k_{crit}(M=0) + \left(\frac{\partial k_{crit}}{\partial M}\right)|_{M=0} \cdot M \tag{1.61}$$

Differentiating eq. (1.56) with respect to M and putting $k = k_{crit}(M=0) = k^0_{crit}$, we find

$$\left(\frac{\partial k_{crit}}{\partial M}\right)|_{M=0} = (s^0_{crit})^2, \tag{1.62}$$

where s^0_{crit} is given by equation (1.58) for $k = k^0_{crit}$:

$$s^0_{crit} = \pm\frac{\sqrt{-F_V G_\theta k^0_{crit}}}{F_V}. \tag{1.63}$$

Plugging eq. (1.62) and (1.63) into (1.61), we finally obtain

$$k_{crit}(M) = k^0_{crit}\left(1 - \frac{G_\theta}{F_V}M\right) \tag{1.64}$$

Evaluating the partial derivatives for the constitutive law $F(V,\theta) = \bar{\sigma}(\mu_* + a\ln\frac{V}{V_*} + b\ln\frac{V_*\theta}{D_c})$ and either the ageing law $G(V,\theta) = 1 - \frac{V\theta}{D_C}$ or the slip law $G(V,\theta) = -\frac{V\theta}{D_C}\ln\frac{V\theta}{D_C}$, we obtain e

$$F_V G_\theta = \frac{\bar{\sigma}a}{D_C}, \qquad\qquad F_\theta G_V = \frac{\bar{\sigma}b}{D_C}. \tag{1.65}$$

Inserting these into eq. 1.60, we obtain a simple expression for k_{crit},

$$k_{crit} = \bar{\sigma}\frac{b-a}{D_C}(1 + \frac{V^2_{pl}M}{a\bar{\sigma}D_c}), \tag{1.66}$$

which is proportional to the coefficient of steady-state friction logarithmic velocity dependence, $b-a$. Note that for velocity-strengthening ($a > b$), we have $k_{crit} < 0$, so in that case we always have $k > k_{crit}$. This means that sliding is always *stable* at the velocity strengthening regime. For velocity weakening ($a < b$), non-linear analysis (Gu et al., 1984), as well as numerical experiments show that for $k > k_{crit}$, the system is stable for small perturbations, but can be made unstable for large perturbations. Consequently, that parameter range is called *conditionally stable.* Finally, for the range $k < k_{crit}$ the system is always *unstable.*

This separation into stability regimes can be extrapolated on geological faults. To do that, an equivalent stiffness k_{eff} of the fault has to be given, which is then compared with k_{crit}. Estimates for this stiffness can be found in Kato (2004) . For example for a square fault of side L with constant slip distance in an infinite elastic medium with shear modulus μ :

$$k_{eff} = \frac{7\sqrt{2}}{3\pi}\frac{\mu}{L}. \tag{1.67}$$

When this expression is compared to k_{crit}, a critical patch size L_c can be defined in the quasi-static regime:

$$L_c = \frac{7\sqrt{2}}{3\pi}\frac{\mu}{(b-a)\bar{\sigma}}D_C. \tag{1.68}$$

According to the stability analysis, seismic slip occurs only if the size of preseismic slip exceeds L_c. When fault is discretized in modeling into smaller patches of constant slip, the size of patches L_p must be smaller than L_c by about an order of ten, otherwise individual patches can reach instability independently on other. The ratio $L^* = L_p/L_C$ is used to distinguish between discrete (for L^* comparable to or greater than one) and continuous ($L^* \ll 1$) models.

1.10 Oscillations

The linear analysis also allows us to find the parameter range for which perturbations will cause oscillations of the system around the steady-state in quasi-static approximation. This will be relevant for our discussion of clock advance later. The system will oscillate if $Im(s) \neq 0$, which is equivalent to $D^2 + 4F_V G_\theta k < 0$. Using equations (1.59) and (1.60) this leads to a condition for k:

$$k^2 + (4F_V G_\theta - 2k_{crit})k + k_{crit}^2 < 0, \tag{1.69}$$

which is satisfied for

$$k_- < k < k_+, \tag{1.70}$$

where

$$k_\pm = -F_V G_\theta - F_\theta G_V \pm 2\sqrt{F_V G_\theta F_\theta G_V}. \tag{1.71}$$

Inserting expressions 1.65 for the partial derivatives, we obtain

$$k_\pm = \frac{\bar{\sigma}}{D_C}(a + b \pm 2\sqrt{ab}) = \frac{\bar{\sigma}}{D_C}(\sqrt{a} \pm \sqrt{b})^2 \tag{1.72}$$

The period T of the oscillations is

$$T = \frac{2\pi}{|Im(s)|} = \frac{4\pi a\bar{\sigma}}{V_{pl}\sqrt{(k_+ - k)(k - k_-)}}, \tag{1.73}$$

where we used that $F_V = \frac{a\bar{\sigma}}{V}$. The oscillations will be exponentially damped or amplified with a characteristic constant h:

$$h = Re(s) = \frac{k_{crit} - k}{2\sigma a}V_p. \tag{1.74}$$

Chapter 2

Presentation of the rate-and-state friction fault model and numerical methods

In this chapter, we describe a formulation in which the evolution of slip on a tectonically loaded fault governed by rate-and-state friction can be modeled and present the numerical methods used.

2.1 Formulation of the problem

We assume an infinite homogeneous isotropic elastic half-space with a (traction-) free surface at its top. The half-space contains a finite rectangular fault interface of width W and height H with an arbitrary orientation with respect to the free surface. The fault is loaded with tectonic plate moving with constant velocity V_{pl}. The angle between the fault and free surface is called *dip*. We orient a Cartesian coordinate system *xyz* so that the fault is defined by conditions $y = 0$ and $0 \leq x \leq W$, $0 \leq z \leq H$. The displacement field $\vec{u}(x, y, z)$ may be discontinuous on the fault - accordingly, we define the *slip vector* $\vec{\delta}$ as

$$\vec{\delta}(x, z) = \lim_{y \to 0^+} \vec{u}(x, y, z) - \lim_{y \to 0^-} \vec{u}(x, y, z). \tag{2.1}$$

We denote the magnitude of the slip vector by δ. Since in our modeling, $\vec{\delta}$ will generally point in only one direction along fault ($\delta_y = 0$), we just use the name *slip* for δ, unless stated otherwise. For convenience, we define $\vec{s}$to be the unit vector parallel to slip, $\vec{s} = \frac{\vec{\delta}}{|\vec{\delta}|}$, and $\vec{n}$ to be the vector normal to our fault, $\vec{n} = \vec{e}_y$. The time derivative of slip is denoted with V and is called the *slip rate,*

slip velocity or just *velocity:*

$$V = \frac{d\delta}{dt}.$$

Let us denote the stress tensor field in the medium by $\boldsymbol{S}(x, y, z, t)$. Outside the fault, we have the equation of local balance of momentum:

$$\nabla \cdot \boldsymbol{S} = \rho \frac{\partial^2 \vec{u}}{\partial t^2} \tag{2.2}$$

(we assume zero body forces). In the quasi-dynamic limit employed here, we assume that the term on the right hand side can be neglected, so eq. (2.2) reduces to

$$\nabla \cdot \boldsymbol{S} = 0. \tag{2.3}$$

The stress tensor is related to the displacement via the generalized Hooke's law:

$$\boldsymbol{S} = (\lambda \nabla \cdot \vec{u})\mathbf{1} + \mu(\nabla \vec{u} + \nabla^T \vec{u}) \tag{2.4}$$

Finally, on the fault, we have an interface condition relating the stress field to friction

$$\tau^{el}(t) + \Delta\tau(t) = \vec{s} \cdot \boldsymbol{S} \cdot \vec{n} = \tau^{fr}(V(t), \theta(t)), \tag{2.5}$$

where we denoted by τ the component of traction parallel to the direction of slip vector, $\Delta\tau(t)$ is an external stress applied on the fault and $\tau^{fr}(V, \theta)$ is the rate-and-state friction given by the constitutive law (1.6):

$$\tau^{fr}(x, z, t) = \sigma(x, z, t) \left(\mu_* + a(x, z) \ln \frac{V(x, z, t)}{V_*} + b(x, z) \ln \frac{V_* \theta(x, z, t)}{D_c(x, z)} \right) \tag{2.6}$$

and the modified ageing law (1.30):

$$\frac{d\theta(x, z, t)}{dt} = 1 - \frac{V(x, z, t)}{D_c(x, z)} \theta(x, z, t) - \frac{\alpha}{b(x, y)} \frac{\dot{\sigma}(x, z, t)}{\sigma(x, z, t)} \theta(x, z, t). \tag{2.7}$$

in which the possible spatial variability of parameters a, b, D_c and the normal stress σ is assumed. In the quasi-static limit, eq. (2.5) would lead to instabilities during modeling. For this reason, a so-called *radiation damping* term is standardly added:

$$\tau^{damp} = -\frac{G}{2\beta} V, \tag{2.8}$$

where G is the shear modulus of the medium and β is the S-wave velocity. This terms has its basis in considering a propagation of a plane S-wave away from the fault. With this term, eq. (2.5) reads

$$\tau^{el} + \tau^{damp} + \Delta\tau = \tau^{fr}. \tag{2.9}$$

We solve the equations (2.3) , (2.9) along with (2.6) and (2.7) numerically as follows. We discretize the fault to $N_W \times N_H$ rectangular patches (or cells) of

dimensions $\Delta x = W/N_W$, $\Delta z = H/N_H$ and impose constant (spatially) slip on the cells, so that:

$$\delta(x,z,t) = \sum_{i=1}^{N_W}\sum_{j=1}^{N_H} \delta_{ij}(t)[\mathcal{H}(x-(i-1/2)\Delta x) - \mathcal{H}(x-(i+1/2)\Delta x)] \times [\mathcal{H}(z-(j-1/2)\Delta z) - \mathcal{H}(z-(j+1/2)\Delta z)], \quad (2.10)$$

where $\mathcal{H}(\cdot)$ is the Heaviside function. The stress field $\boldsymbol{S}$ arises due to the presence of slip on these patches and can be calculated as a linear superposition of contributions from each patch. To calculate these contributions, we use the subroutine DC3D coded by Y. Okada that lets us calculate the static displacement field $\vec{u}_{kl}(x,y,z)$ and its spatial derivatives due to slip on any generally inclined rectangular cell c_{kl} at any point (x,y,z), in an elastic half-space bounded by a (traction-) free surface. The displacement field derivatives can be converted into stress using Hooke's law (2.4) and the resulting stress field $\boldsymbol{S}_{kl}(x,y,z)$ will then satisfy the equation (2.2). In our calculations, we are only interested in stresses induced on the fault. We denote the stress at the center of cell c_{ij} arising due to slip at cell c_{kl} as $\boldsymbol{S}_{ij,kl} = S_{kl}\left(x+(i-1/2)\Delta x, 0, z+(j-1/2)\Delta z\right)$ and we denote by $\tau_{ij,kl}$ the corresponding component of traction parallel to slip, $\tau_{ij,kl} = \vec{n}\cdot\boldsymbol{S_{ij,kl}}\cdot\vec{s}$. To get the total traction $\tau_{ij} = \tau\left(x+(i-1/2)\Delta x, 0, z+(j-1/2)\Delta z\right)$ induced at cell c_{ij} we sum over the contributions from all the cells on fault:

$$\tau_{ij} = \sum_{k,l} \tau_{ij,kl} \quad (2.11)$$

The traction $\tau_{ij,kl}$ is proportional to the slip on cell c_{kl}. If we define $K_{ij,kl}$ to be the traction at c_{ij} arising due to unit slip at c_{kl}, then we can write:

$$\tau_{ij,kl} = K_{ij,kl}\delta_{kl} \quad (2.12)$$

(no summation over repeating indices is assumed). For total traction at c_{ij}, we have

$$\tau_{ij} = \sum_{k,l} K_{ij,kl}\delta_{kl}. \quad (2.13)$$

The set of numbers $K_{ij,kl}$ is called *the kernel.* The subroutine DC3D is invoked only once, at program execution, to calculate the kernel. During the program run, the tractions τ_{ij} are then calculated via eq. (2.13). On each cell, we solve the discretized interface condition

$$\tau_{ij}(t) = \tau_{ij}^{fr}\left(V_{ij}(t), \theta_{ij}(t)\right), \quad (2.14)$$

where τ_{ij}^{fr} is discretized in the same way as τ_{ij}. Plugging in we get a set of equations:

$$\sum_{k,l} K_{ij,kl}\left(\delta_{kl}(t) - V_{pl}t\right) - \frac{G}{2\beta}V + \Delta\tau_{ij} = \sigma_{ij}(t)\left(\mu_* + a_{ij}\ln(\frac{V_{ij}(t)}{V_*}) + b_{ij}\ln(\frac{V_*\theta_{ij}(t)}{D_c})\right) \quad (2.15)$$

and

$$\frac{d\theta_{ij}(t)}{dt} = 1 - \frac{V_{ij}(t)}{D_{c,ij}}\theta_{ij}(t) - \frac{\alpha}{b_{ij}}\frac{\dot{\sigma}_{ij}(t)}{\sigma_{ij}(t)}\theta_{ij}(t). \tag{2.16}$$

Differentiating (2.15) with respect to time and putting dV/dt on the left hand side, we obtain

$$\frac{dV_{ij}(t)}{dt} = \frac{\sum_{k,l} K_{ij,kl}(V_{ij}(t) - V_{pl}) - \sigma_{ij}(t)\frac{b_{ij}}{\theta_{ij}(t)}\frac{d\theta_{ij}(t)}{dt} - \mu_{ij}(t)\dot{\sigma}_{ij}(t) + \Delta\dot{\tau}_{ij}(t)}{\frac{\sigma a}{V} + \frac{G}{2\beta}}. \tag{2.17}$$

The equations (2.16) and (2.17) can be written as a system of differential equations of type:

$$\frac{d\vec{y}}{dt} = \vec{f}(\vec{y}, t). \tag{2.18}$$

This system can be integrated using an explicit Runge-Kutta scheme. We make use of a Runge-Kutta algorithm with a fifth-order adaptive step-size control coded by Press et al. (1997) .

2.1.0.1 Simplifications

For a certain class of faults, the kernel $K_{ij,kl}$ enjoys symmetries that allow a faster computation of the derivatives given by (2.17).. If two sides of the fault are parallel with the surface, then there is a translational symmetry along the fault's width, so the dependence of $K_{ij,kl}$ on indices i and k must appear as a difference $i-k$. The sum $\sum_{k,l} K_{ij,kl}(V_{ij}(t)-V_{pl})$ then changes to convolution in one of the indices and can be solved with a 1-D discrete Fourier transformation. If the effect of free surface is neglected (for example at large depths), then we also have translational symmetry in indices j and l and the sum simplifies to a convolution in both indices, which can be solved with a 2-D discrete Fourier transform.

In the case of strike-slip fault (with $dip = 90^o$), we calculate the kernels at large depth and then replicate the free-surface effect by adding velocities symmetric with respect to the surface. This allows the use of 2-D DFT even in the presence shallow depths.

Chapter 3

Fault seismicity modeling

Here, we use the method described in previous chapter to model the effect of distributions of heterogeneous parameters on fault seismicity.

3.0.1 Frequency-size distribution

One of the important questions concerning the applicability of the rate-and-state laws in numerical modeling of fault seismicity is their ability to reproduce empirical statistical behavior exhibited by natural faults. Specifically, the model should be able to reproduce the Gutenber-Richter (GR) frequency-magnitude distribution (at least in a limited range of magnitudes) observed in real faults. The law posits that the relationship between magnitude M and total number of earthquakes $N(M)$ with magnitude larger than M follows a power law

$$N(M) = 10^{a-bM}, \tag{3.1}$$

, where a and b are parameters. The value of b is very close to one (see e.g. Morgan, 2015) . This relation is more commonly expressed in a logarithmic form

$$\log_{10} N = a - bM. \tag{3.2}$$

If the model is able to reproduce the Gutenberg-Richter (GR) distribution, we can ask more specific questions: Does this ability depend on the spatial distribution of model parameters, or does it follow naturally from the nonlinear dynamics contained in the frictional laws (e.g. would it be possible to reproduce GR distribution even for homogeneous faults)? This question was first explored by Rice (1993) for a fault whose parameters varied in only one dimension . He showed that spatio-temporal complexity is a feature of models with low resolution and disappears as the discretization improves. However, Rice used a fault with a deterministic, piecewise linear distribution of frictional parameters, so it wasn't obvious if GR seismicity would not emerge naturally from faults with more complex distributions.

Since GR distribution is a power law, it may be expected that it should appear on faults with fractal distributions of friction - see Newman (2004) for a

nice overview of the relationship between power laws and scale invariance, as well as a discussion of some mechanism by which power laws can arise. A number of authors have published models with fractal distribution of frictional parameters that exhibit GR. However Lapusta (2000) noted that their complexity was also due to the insufficient discretization of the faults, rather than spatial complexity.

In this thesis, we are naturally interested in this question, because without a model able to generate Gutenber-Richter event distribution in at least a limited range of magnitudes, we cannot expect the results to be very realistic. For this reason, we generated a large number of models with (pseudo-) random distributions of frictional parameters and wrote a code to extract seismic catalogs. We hoped that this could let constraint the parameters of fault model to realistic values. Unfortunately, other than the effect of discretization, we found no systematic dependence of seismicity on the model setup.

3.0.2 Extraction of earthquake catalog

In order to statistically describe seismicity on the fault, we extract a seismic catalog using similar criteria to those described by Hillers et al. (2006). We break the slip velocity history into separate *events* which serve as our basic statistical units. One event comprises of active cells which share a common hypocenter. Cells c_j are active at time t if their velocity $V_j(t)$ is greater than a given threshold value V_{trs}. More formally, at any given time t, a cell c_i belongs to event e_k iff any of these two conditions hold:

1. c_i is the hypocenter of e_k (i.e. there was a time $t_h \leq t$ at which $V_i(t_h) > V_{trs}$, c_i or any of its neighbors weren't part of any other event and the number of hypocenters was $k-1$) and the slip rate on c_i was larger than V_{trs} for all times t_p satisfying $t_h \leq t_p \leq t$.

2. c_i was in contact with another cell belonging to e_k at some time $t_c \leq t$ and the slip rate on c was larger than V_{trs} for all times t_p satisfying $t_c \leq t_p \leq t$.

A cell can at any time belong to more than one event, but if that happens for any cell then we treat the events as single one (merge them together) and assign them the index of the oldest event (for example, if an active cell belonging to e_l meets with an active cell belonging to event e_m, $l \neq m$, then we formally treat the two events as a single event $e_{min(l,m)}$).

For each event the following quantities are recorded:

- Nucleation time t_h and hypocenter coordinates x_h, y_h.
- The time t_e in which the number of the event cells went to zero, and the event duration $\Delta t = t_e - t_h$
- The *seismic moment* M_0 defined as $M_0 := \mu \int_{t_h}^{t_e} dt \int_{S(t)} dS\delta(\mathbf{x}, t)$, where μ is the shear modulus and $S(t)$ is the surface of the event at time t.

Numerically, this just amounts to $M_0 = \mu\delta\Delta x\Delta z$, where δ is the total slip undergone over the event history.

- The *moment magnitude* M_w, introduced by Hanks and Kanamori M_0 : $M_w = \frac{2}{3}log_{10}M_0 - 6.07$
- The maximum current number of cells N_{max} (i.e. the maximal number of active cells belonging to the event at any given time) and the total number of active cells N_{tot}.

3.0.3 Generation of random parameters

To generate heterogeneous random parameters, we use a method described by Klimeš (2002). First, we use a pseudo-random generator to create distributions that are samples of the uniform probability distribution on the unit interval, $U(0, 1)$. If samples of normal distribution are desired instead, we apply the Box-Muller transformation to achieve this. This way, we obtain a two dimensional array of parameters $p(i, j)$. We then apply the 2-D discrete Fourier transform to obtain a distribution $\hat{p}(k_1,k_2)$. The result is then multiplied by an isotropic spectral filter of the form

$$\hat{f}(k) = \hat{f}_{S_N}(k)\hat{f}_c(k)\hat{f}_{a_G}(k) \tag{3.3}$$

where $k = k_1^2 + k_2^2$ and

$$\hat{f}_{S_N}(k) = k^{-1-N} \tag{3.4}$$

is the self-affine filter,

$$\hat{f}_c(k) = \left[1 + (ck)^{-2}\right]^{-(1+N)/2} \tag{3.5}$$

is a high-pass wavenumber filter and

$$\hat{f}_{a_G}(k) = \exp\left(-\frac{a_G^2 k^2}{8}\right) \tag{3.6}$$

is a low-pass wavenumber Gaussian filter. The parameters N, c and a_G are called the *Hurst exponent, von Kármán correlation length* and *Gaussian correlation length* respectively. Klimeš (2012) notes that the Hurst exponent in the range $-1/2 < N < 0$ is suitable for use in geological structures, so we confine ourselves to that range. The resulting product is then transformed back into the time-domain and a normalization is applied so that the maximum of the distribution is equal to a prescribed value p_{max}. Finally, the parameters are superimposed upon a deterministic parameter background.

3.0.4 Searching for models providing realistic seismicity

We performed a large number of tests with frictional parameters changing up to 50%. At the beginning of each test, we set the $V = 1.5V_{pl}$ and $\theta = \theta_{SS}(V_{pl}) =$

$\frac{D_C}{V_{pl}}$ everywhere on the fault. This homogeneous initial condition was used to eliminate effects of arbitrary velocity distribution in models with random distributions of parameters. Then we performed simulations of 1000 years of fault evolution.

We found that adding self-similar distributions by itself does not guarantee a power law distribution. In fact, for most of the distributions we used, we were unable to generate GR distributions, and we found almost no systematic dependence of the generated seismicity and the parameters of the random distributions of the frictional parameters. We found two effects worth mentioning - 1) creating GR models is easier when uniform, rather than Gaussian, initial (unfiltered) distribution of parameters is used and 2) the frequency-size distributions tend to exhibit power law behavior in a limited range when smaller number of cells is used and the slope of the power law part tends to get steeper as the number of cells is decreased. Both of these effects were previously described by Hillers et al. (2006) . We specifically show the effect of discretization in the next subsection.

Here we present some examples of frequency-size distributions that are illustrative of the typical results we found. We plot the graph of event locations, their frequency-size distributions and a graph of events vs time.

In Figure 3.1 we plot a histogram with a periodically repeating event of magnitude 6.7 nucleating at the center of the fault. Such seismicity was always seen in homogeneous models with no random parameters. However, it was also seen in some stochastic models, especially for denser discretizations.

In Figure 3.2, there are small ranges of magnitudes in which a power law behavior (albeit with $b < 1$) is obeyed for a few large events. This kind of "broken" seismicity was typical for a large number of our models - the large events occur periodically and the smaller events can be understood as the foreshocks or aftershocks of these. This behavior of smaller events clustering together in time around a large events was seen in almost all models we tested.

In Figure 3.3 we show seismicity obeying GR dependence with $b = 1$ in a limited range of 2 magnitudes (from 3-5). We were not able to produce G-R seismicity in a large range than this. The only way a power law $b = 1$ could be created was by using smaller discretization then corresponds to a continuum limit defined by the requirement that $max(\Delta x, \Delta z) \ll L_C$, for L_C defined in eq. (1.68). In the picture shown we have a fault of $35x35\ km^2$ discretized in 128×128 cells, which corresponds to $max(\Delta x, \Delta z)/L_C = 0.4$. If the discretization is increased, then power law behavior is preserved, but the slope and the total number of events decreases. From the plot of magnitude on time, it can be seen that smaller events are once again clustered around the large ones. We were not able to generate GR seismicity without this clustering.

A rare example of seismicity with events that are not temporally clustered can be seen in figure 3.4. This seismicity was produced by a fault with two velocity-weakening zones separated from each other by velocity-strenghtening zones. We can see that the events occur almost continuously, with magnitudes ranging from 2 to 7. However, power law seismicity is not observed.

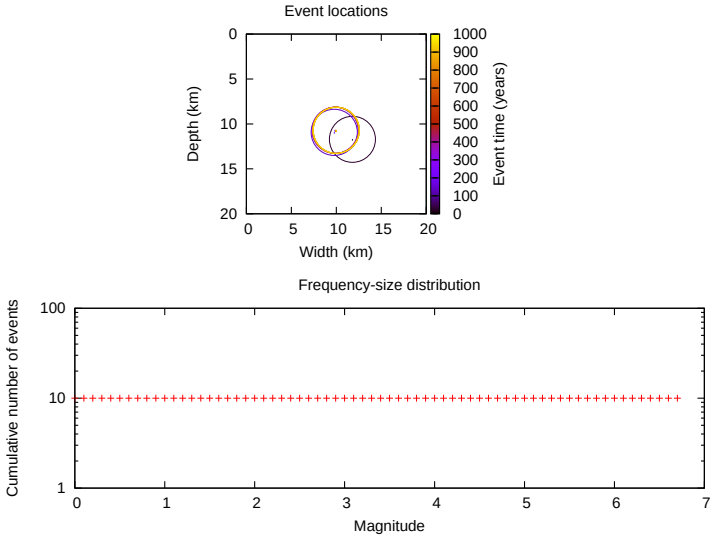

(a)

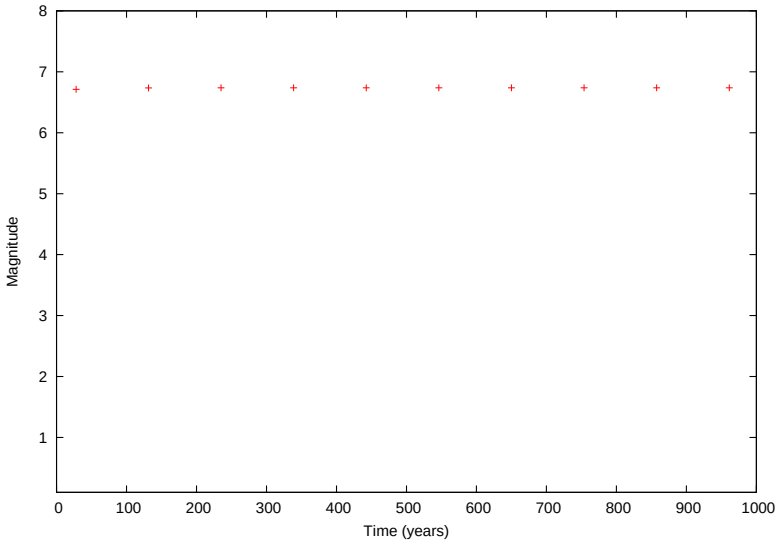

(b)

Figure 3.1: Seismicity comprised of a single repeating event: a) Event locations and the frequency-size distribution, b) A plot of magnitudes vs time. The size of the circles in the graph scales with magnitude., while the color represents the hypocenter time (see color scale).

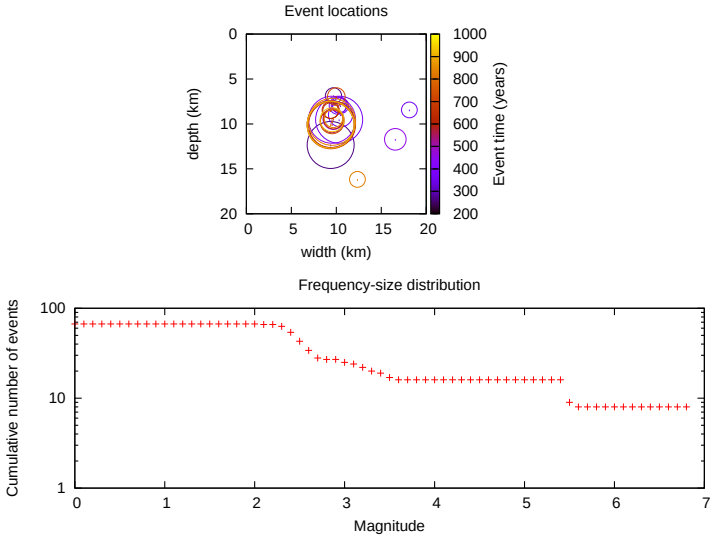

(a)

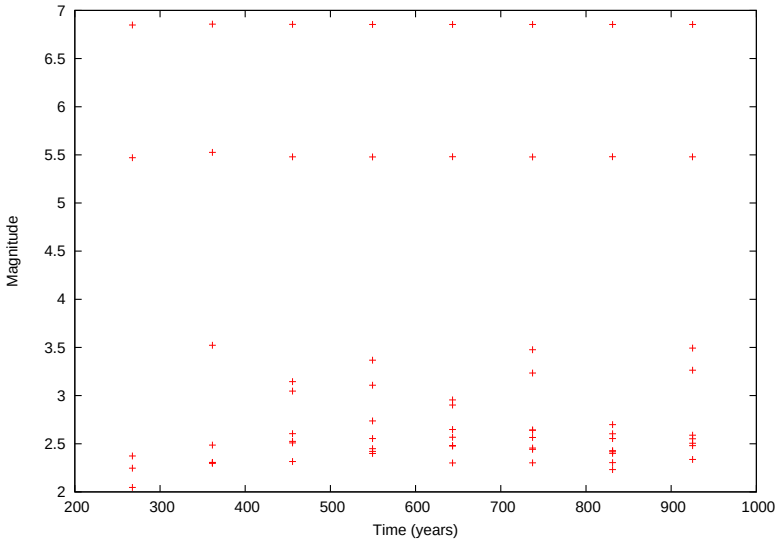

(b)

Figure 3.2: Seismicity containing power laws in two very short ranges of smaller magnitudes and a small number of characteristic large events: a) Event locations and the frequency-size distribution, b) A plot of magnitudes vs time. The size of the circles in the graph scales with magnitude., while the color represents the hypocenter time (see color scale).

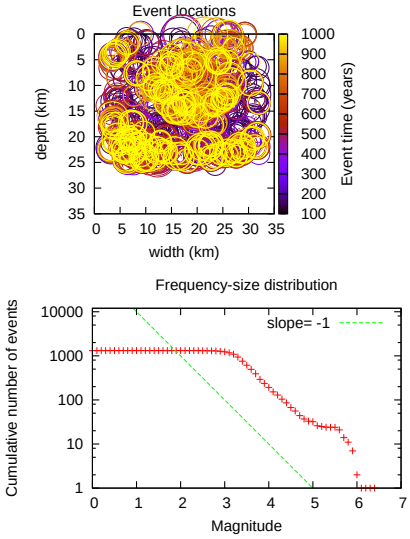

(a)

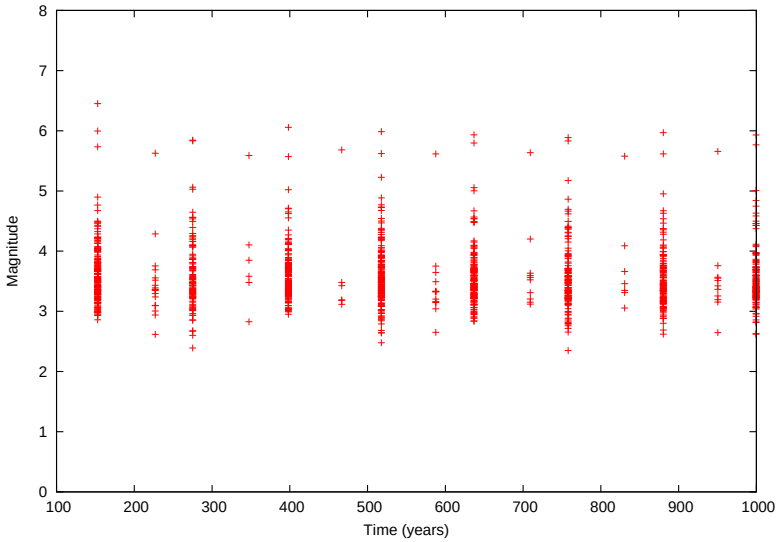

(b)

Figure 3.3: Seismicity obeying the G-R in a limited range of 2 magnitudes: a) Event locations and the frequency-size distribution, b) A plot of magnitudes vs time. The size of the circles in the graph scales with magnitude., while the color represents the hypocenter time (see color scale).

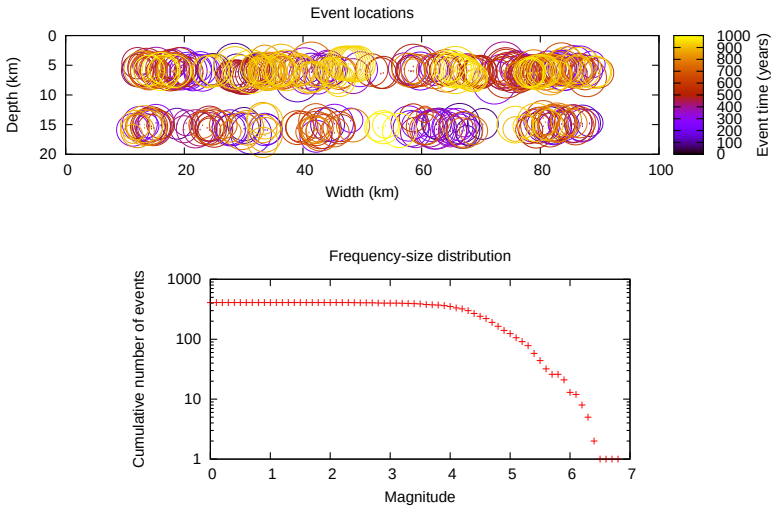

of

(a)

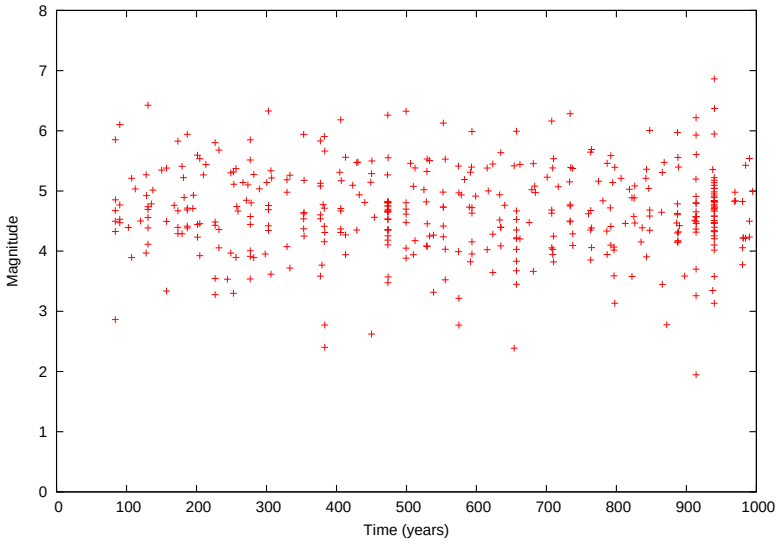

(b)

Figure 3.4: Seismicity with negligible interseismic periods.: a) Event locations and the frequency-size distribution, b) A plot of magnitudes vs time. The size of the circles in the graph of event locations corresponds to magnitudes, while the color represents the event time.

3.0.5 (In)dependence on realization

An interesting question regarding the seismicity in stochastic models is whether or how much the resulting seismicity depends on the concrete realization of random distribution - if the parameters of spectral filter a, N are the same, will different realizations change seismicity? To study this we choose a strike-slip fault of 25×25 km with 128×128 cells. The fault has a homogeneous parameter background distribution of $a = 0.015$, $b = 0.019$ and $D_C = 2$ cm, to which we add random distributions b_{rand} of the parameter b in the range $-0.004 < b_{rand} < 0.004$ (we tried varying the parameters a and D_C as well with same results) . We chose the Hurst parameter $N = -0.2$ and test three different correlation lengths $c = 0.001$ km (which is much less than the size of individual cells $\Delta x = \Delta z = 0.19$ km, so this essentially amounts to white noise), $c = 0.58$ km and $c = 11$ km to study the possible effect of correlation length (we could expect that the differences will be greater for larger correlation lengths rather than for the smaller ones). Example realization for each correlation length is shown is shown in figure 3.5. The histograms are shown in figure 3.6. We can see that regardless of the correlation length used, the seismicity does depend on realization. The total number of events can vary by more than a factor of 10. However, the slope of falling part of histogram is approximately the same for each realization.

3.0.6 The effect of discretization

Could the dependence of seismicity on concrete realizations change with discretization used? To answer this question, we choose a fault of dimensions $20x20$ km and generated 4 realizations of random b values with $c = 0.58$ km for discretizations of 16×16, 32×32, 64×64, 128×128 and 256×256 cells. The result can be seen in figure 3.7. Note that since the y-axis is in logarithmic scale, curves that are a constant distance apart are actually related by a constant ratio. We can see that the graphs are practically realization independent in the $16x16$ case. For higher discretizations, the logarithmic differences are approximately the same for each discretization - this means that the relative differences in total number of events are about the same. Since less events are generated for the higher discretizations, this means the absolute differences are smaller. To compare other differences, we collapsed the curves so that they overlap in the "flat" part, i.e. we normalize them to have the same total number of events . The resulting graph is plotted in figure 3.8. With this correction, we may observe that the difference in slopes is small for small resolutions and increases with higher resolutions. This is also the case for

In another test of discretization, we took a homogeneous fault with $a = 0.015$,$b = 0.015$,$D_C = 0.02$ with dimensions $40x40$ km and applied a random distribution of D_C of various correlation lengths. In figure 3.9 we show a typical realization of D_C for $c = 20km$. The typical effect of discretization is shown in figures 3.9-3.11. As the discretization increased, the steepness of cumulative histograms (in log-scale) decreases - b is about 2.30 for the 64x64 case and 0.23

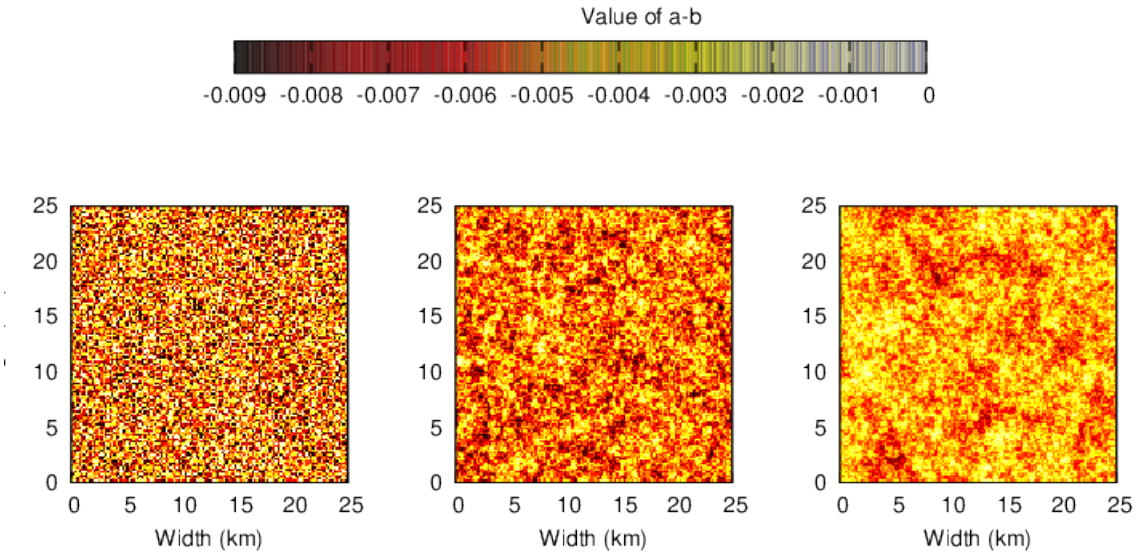

Figure 3.5: Example realizations of distribution of $a - b$ for three different correlation lengths: $c = 0.001$,0.58 and 11 km (from left to right).

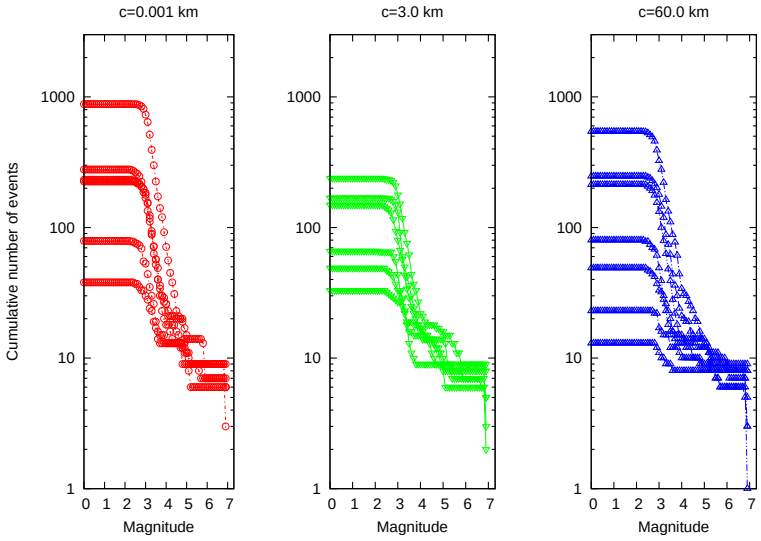

Figure 3.6: Histograms for six different realizations for each correlation length - $c = 0.001$,0.58 and 11 km, from left to right.

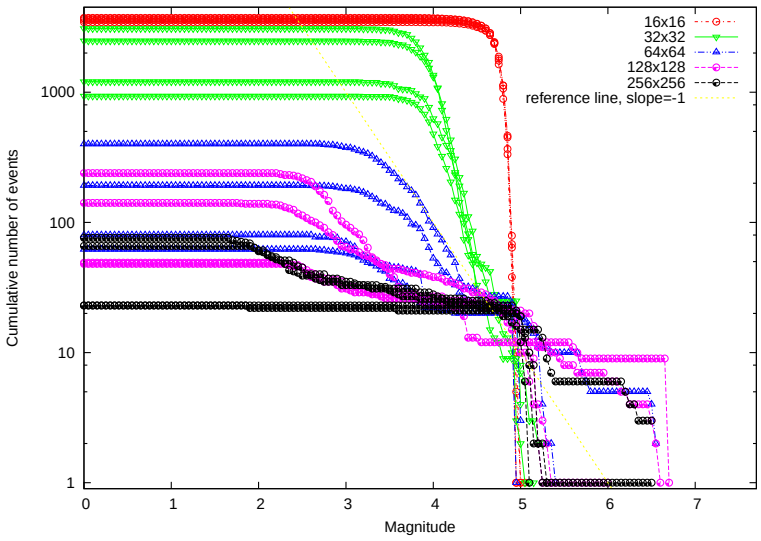

Figure 3.7: Histograms for various discretizations and different realizations of the uniform distribution. Matching discretizations are designated by colors.

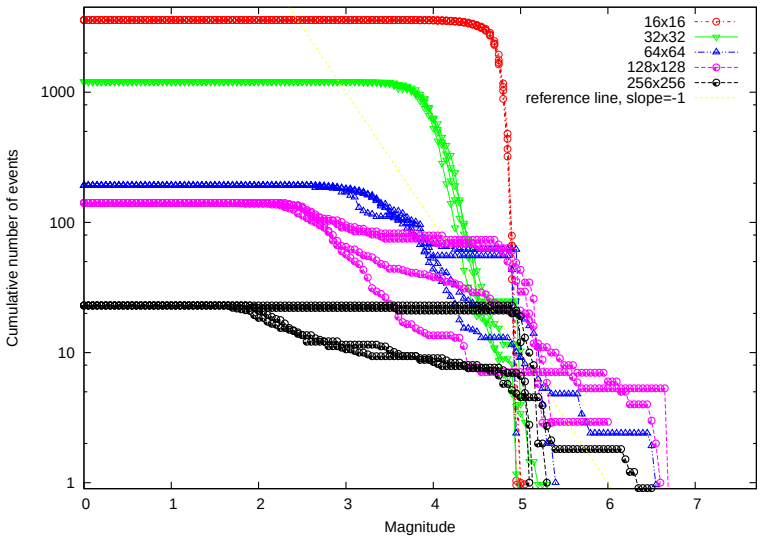

Figure 3.8: Same as figure 3.7 but the histogram corresponding to each discretization are collapsed together so that the difference in slopes can be seen

x(etc.)

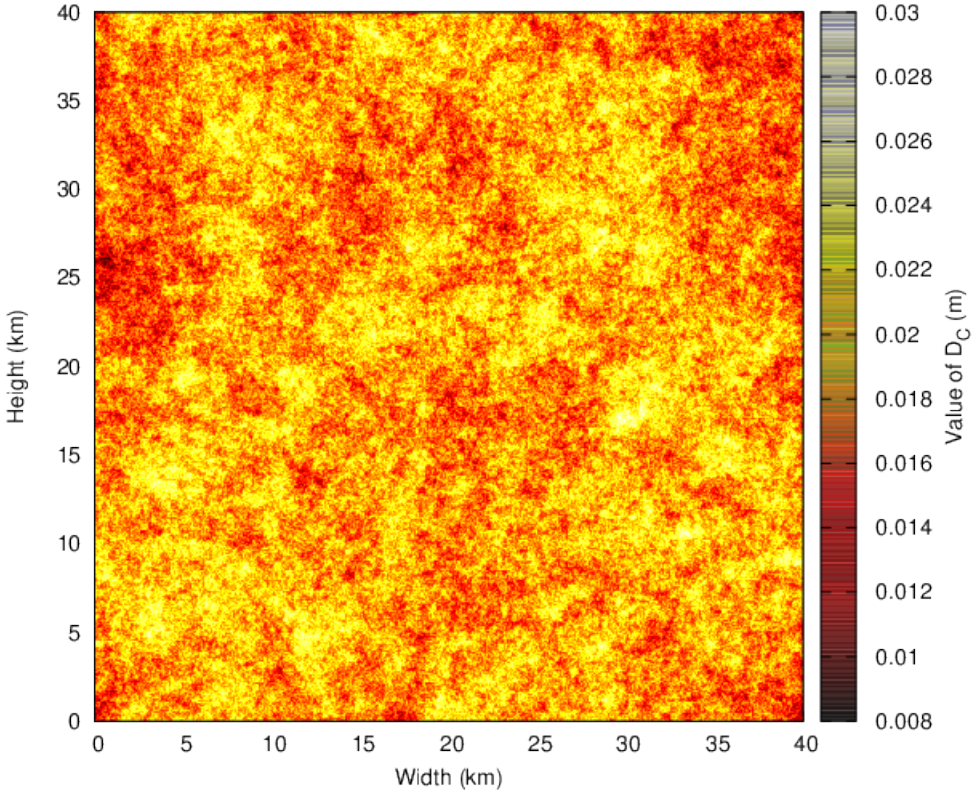

Figure 3.9: Distribution of L parameters for the discretization experiment. The case for 512x512 cells is shown.

for the 512x512 case (we give only approximate values, since the value of b depends on the range of points in which the fit is made). The total number of events also decreases and smaller events are more prevalent in the more resolved case - for each resolution, there's a cutoff magnitude below which no event appears, this value of this cutoff decreases with resolution. However, for all resolution, the largest magnitude is the same (7.35 in this case). From the figure 3.11 we can see that the events for smaller discretization nucleate across a large area of the fault, whereas for the large discretization, there's a few large events. The smaller events are temporal clustered around the large ones.

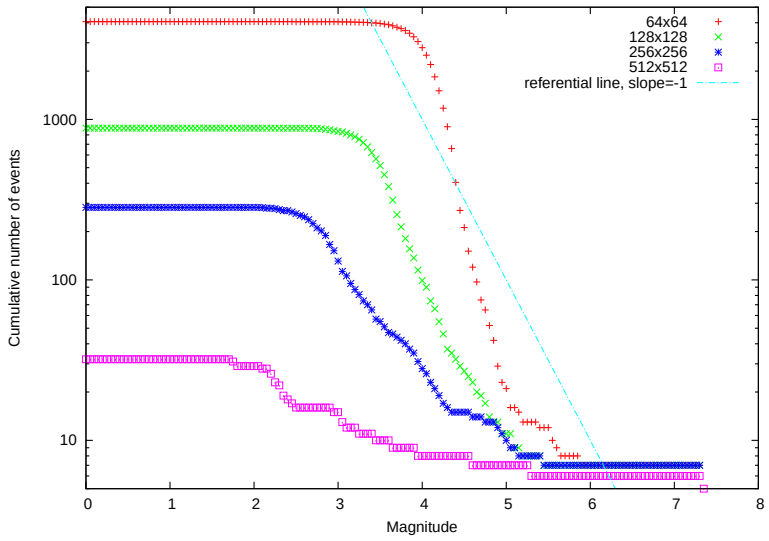

Figure 3.10: Cumulative number of events for different discretizations of the fault with varying D_C.

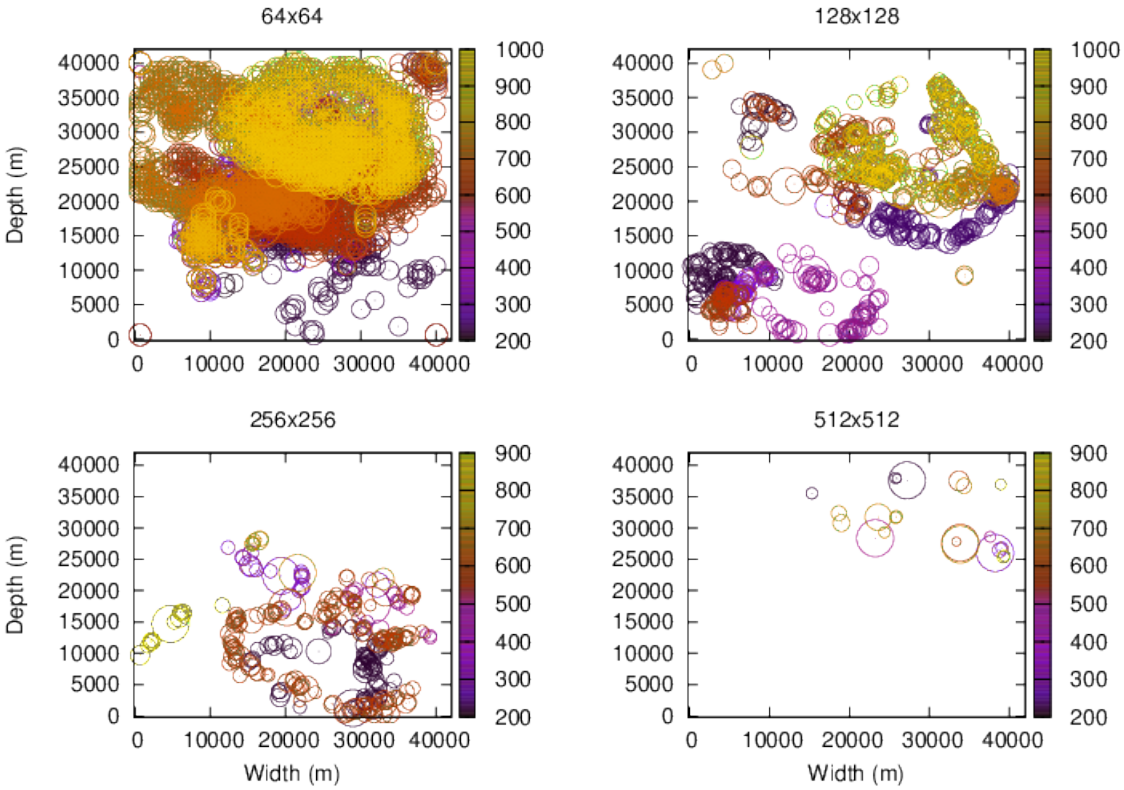

Figure 3.11: Locations of events for each distribution in the discretization experiment. Color is used to depict event times (in years).

Chapter 4

The effect of Coulomb stress change on clock advance

In this chapter, we study the effect of external changes in both the shear and normal stress on the seismicity of a rate-and-state governed fault. Of particular interest to us are the changes in nucleation time of events. Let assume that, in absence of any external stress changes ($\Delta\tau(t) = 0$), an event will nucleate at time t_f. In the presence of external shear stress change $\Delta\tau(t)$ and normal stress change $\Delta\sigma(t)$, the next event will instead nucleate at time t_p. In accordance with previous use by Perfettini (2003), we define *clock advance* CA as $CA = t_f - t_p$. The combination $\Delta\tau - \mu_*\Delta\sigma$ is called the Coulomb stress change.

4.1 Clock advance formula

In this section, we follow Perfettini et. al. (2003) to derive a formula for clock advance due to stress perturbation for a spring slider model. We modify his derivation by taking into account a case of weakly varying normal stress. During the locked phase of the earthquake cycle, the radiation damping term may be neglected. In the presence of (in general time dependent) shear stress perturbation, the equation 1.47 changes to

$$\tau(t) = \tau_0 + k(V_{pl}t - \delta(t)) + \Delta\tau(t) \tag{4.1}$$

Recall that we also have, from the friction constitutive law

$$\tau(t) = \sigma(t)\left(\mu_* + a\ln(\frac{V(t)}{V_*}) + b\ln(\frac{V_*\theta(t)}{D_c})\right) \tag{4.2}$$

The state variable satisfies the modified version of Dieterich's aging law (1.30):

$$\frac{d\theta(t)}{dt} = 1 - \frac{V(t)}{D_c}\theta(t) - \frac{\alpha}{b}\frac{\dot{\sigma}(t)}{\sigma(t)}\theta(t) \tag{4.3}$$

Assuming that $V(t) = \frac{d\delta(t)}{dt}$ and $\sigma(t)$ is known, (4.3) is a linear differential equation of first order in θ. It has the solution

$$\theta(t) = K\exp(-\frac{\delta(t)}{D_c})\sigma(t)^{-\frac{\alpha}{b}}\,(1 + C(t)) \tag{4.4}$$

where

$$C(t) = \frac{1}{K}\int_0^t exp(\frac{\delta(t')}{L})\sigma(t')^{\frac{\alpha}{b}}dt') \tag{4.5}$$

and

$$K = \theta(0)\exp(\frac{\delta(0)}{D_C})\sigma^{\frac{\alpha}{b}}(0). \tag{4.6}$$

Inserting this expression into (4.2) and setting expressions (4.1) and (4.2) equal, we obtain

$$\begin{aligned} &a\sigma(t)\ln\frac{V}{V_*} = \tau_0 + k(V_{pl}t - \delta) + \Delta\tau(t) - \\ &-\sigma(t)\left(\mu_* + b\ln\left(\frac{V_*}{D_c}\theta(0)\right) + b\frac{\delta(0)}{D_C} - \alpha\ln\left(\frac{\sigma(t)}{\sigma(0)}\right) - b\frac{\delta(t)}{D_c} + b\ln\left(1 + C(t)\right)\right), \end{aligned} \tag{4.7}$$

or, solving for V

$$\begin{aligned} V(t) = V_*\exp\left(\frac{\tau_0}{a\sigma} - \frac{\mu_* + b\ln\left(\frac{V_*}{D_c}\theta(0)\right)}{a}\right)\exp\left(\frac{kV_{pl}t + \Delta\tau}{a\sigma}\right)\exp(\frac{-k\delta(t)}{a\sigma})\times \\ \times\left(\frac{\sigma(t)}{\sigma(0)}\right)^{\frac{\alpha}{a}}\exp(\frac{b}{a}\frac{\delta(t) - \delta(0)}{D_c})\,(1 + C(t))^{-\frac{b}{a}}, \end{aligned} \tag{4.8}$$

Assuming that $\Delta\tau(0) = 0$, for $t = 0$ this reduces to

$$V(0) = V_*\exp\left(\frac{\tau_0}{a\sigma} - \frac{\mu_* + b\ln\left(\frac{V_*}{D_c}\theta(0)\right)}{a}\right)\exp(\frac{k\delta(0)}{a\sigma}), \tag{4.9}$$

so equation (4.8) can be written as

$$\begin{aligned} V(t) = V(0)\exp\left(\frac{kV_{pl}t + \Delta\tau(t)}{a\sigma}\right)\exp(\frac{H(t)\bar{\delta}(t)}{a})\times \\ \times\left(\frac{\sigma(t)}{\sigma(0)}\right)(1 + C(t))^{-\frac{b}{a}}, \end{aligned} \tag{4.10}$$

where $\bar{\delta}(t) = \delta(t) - \delta(0)$ and $H(t) = \frac{b}{D_c} - \frac{k}{\sigma(t)}$. At this point, let us suppose that $\sigma(t) = \sigma_0 + \Delta\sigma(t)$ does not change significantly, so that $\frac{dH}{dt} = \frac{k\Delta\dot{\sigma}}{(\sigma+\Delta\sigma(t))^2} \approx 0$ and $H(t)$ is approximately constant, $H(t) = H$. Rearranging (4.10) and integrating over time, we obtain

$$\int_0^t V(t') \exp(-\frac{H\bar{\delta}(t')}{a})dt' = F(t), \tag{4.11}$$

where $F(t)$ is defined by :

$$F(t) = \int_0^t V(0) \exp\left(\frac{kV_{pl}t' + \Delta\tau(t')}{a\sigma}\right)\left(\frac{\sigma(t')}{\sigma(0)}\right)^{\frac{\alpha}{a}} (1 + C(t'))^{-\frac{b}{a}}\, dt'. \tag{4.12}$$

Noting that $V(t) = \frac{d\delta(t)}{dt} = \frac{d\bar{\delta}(t)}{dt}$, we can analytically calculate the integral on the left-hand of (4.11) side to obtain a constraint for $\bar{\delta}(t)$

$$\bar{\delta}(t) = -\frac{a}{H}\ln\left(1 - \frac{HF(t)}{a}\right). \tag{4.13}$$

Differentiating this with respect to time, we receive

$$V(t) = \frac{dF/dt}{1 - \frac{HF(t)}{a}}. \tag{4.14}$$

During the time of instability t_p, the slip rate goes to infinity $V(t) \overset{t\to t_p}{\to} \infty$, so t_p must satisfy the equation

$$F(t_p) = \frac{a}{H}. \tag{4.15}$$

4.2 Consequence of the instability time formula

The time to instability t_p is given by the equation 4.15 and it is, in general, not possible to find an explicit analytic solution. However, a couple of interesting things may be drawn. First, note that the integrand in equation 4.12 is positive, so$F(t)$ is also positive for $t > 0$. Since a is positive, this means that the equation 4.15 has solution only if $H(t_p) > 0$. From the definition of H, this is equivalent to

$$\frac{b}{D_c} > \frac{k}{\sigma_0}. \tag{4.16}$$

If this condition is not met then no instability can occur.

Next, the positivity of the integrand translates into $dF/dt > 0$. Since $V(t) > 0$, this means that the denominator in equation (4.14) must also be positive, so $F(t)$ must be bounded from both sides for all $0 < t < t_p$:

$$0 < F(t) < F(t_p) = \frac{a}{H} \tag{4.17}$$

Let us consider the dependence of F on parameters β (such as a, b, D_c, σ_0, etc.). Defining a function S with

$$S(t, \beta) := F(t, \beta) - \frac{a}{H}, \tag{4.18}$$

eq. (4.15) can be written as

$$S(t_p, \beta) = 0. \tag{4.19}$$

By the implicit function theorem, we have

$$\frac{dt_p}{d\beta} = -\frac{\frac{\partial S}{\partial \beta}}{\frac{\partial S}{\partial t_p}}. \tag{4.20}$$

Now, since $\frac{\partial S}{\partial t_p} = \frac{\partial S}{\partial t_p} > 0$ it follows that $\frac{dt_p}{d\beta} < 0$ if $\frac{\partial S}{\partial \beta} > 0$ and $\frac{dt_p}{d\beta} > 0$ if $\frac{\partial S}{\partial \beta} < 0$. In other words, if S increases with β than the time to instability decreases with β and vice-versa. For example, from the definitions of F and H, we can see that S increases with the amplitude of $\Delta\tau$, V_{pl} or k. The spring-slider formula thus predicts that increasing these parameters will bring decrease the time to failure, while decreasing them will increase it.

Perfettini also derived a closed expression for t_p for the case of pure shear-stress step later in the earthquake cycle:

$$t_p = -\frac{\Delta\tau}{kV_{pl}} + \frac{1}{\gamma} \ln \left[1 + \frac{\gamma a}{\dot{\delta}(0) H} - \exp(\gamma t_0)(1 - \exp[\Delta\tau/(a\sigma_0)]) \right], \tag{4.21}$$

where $\gamma = kV_{pl}/(a\sigma_0)$. For $\Delta\tau = 0$, this leads to an estimate of *the free* (unperturbed) duration t_f of earthquake cycle:

$$t_f = \frac{1}{\gamma} \ln \left(1 + \frac{\gamma a}{\dot{\delta}(0) H} \right) \tag{4.22}$$

Consequently, a formula for clock advance is $CA = t_f - t_p$ is given:

$$CA = \frac{\Delta\tau}{kV_{pl}} - \frac{1}{\gamma} \ln \left[1 - \frac{\exp(\gamma t_0)(1 - \exp[\Delta\tau/(a\sigma_0)])}{1 + \frac{\gamma a}{\dot{\delta}(0) H}} \right]. \tag{4.23}$$

4.3 Modeling the effect of Coulomb stress change

4.3.1 Homogeneous fault

In the first set of tests, we took a completely homogeneous fault in the velocity weakening parameter range and placed it in great depth to avoid the free surface effect (3000 km although this is certainly much more then necessary). This allows us to focus on the effect of the properties of Coulomb stress change (i.e. amplitude, placement, duration, etc.) themselves, without spoiling them with the effect of parameter heterogeneity or free surface. We look at the influence of these later. The dimensions of the fault are 25×25 km^2 and we use 128×128

cells. The parameters of the fault are $\mu_* = 0.6$, $a = 0.015$, $b = 0.019$,$D_C = 2$ cm, $\alpha = \mu_*/3 = 0.2$, $V_* = 10^{-6}$ m, $\sigma_0 = 75$ MPa, $\lambda = 20$ GPa, $\mu = 30$ GPa,$\beta = 3$ km/s and $V_{pl} = 3.5$ cm/year. After one or two earthquakes, the fault reaches a stable cycle of repeating events, the graphs of maximum and average velocity and average slip vs time are shown in fig. 4.1. In fig. 4.2 we plotted snapshots of the velocity field normalized with plate velocity V/V_{pl} at the beginning of earthquake cycle ($t = 16$ years) and near the end ($t = 72$ years) (different color scale is used in each picture). Snapshots of earthquake nucleation were plotted in fig. 4.3

The duration t_f of the unperturbed interseismic cycle in our setup is 89 years. We set the time coordinate to $t = 0$ at the beginning of the $8th$ earthquake cycle (During time interval $< t_0, t_0 + \Delta t >$ we apply a perturbation of $\Delta\tau$ of the form

$$\Delta\tau(t) = \frac{1}{2}A\left[1 - \cos\left(\pi\frac{t - t_0}{\Delta t}\right)\right], \tag{4.24}$$

which is an increasing function of time, for which $\Delta\tau(t_0) = 0$ and $\Delta\tau(t_0+\Delta t) = A$. Here, A is the amplitude of the stress change. With the exception of one experiment, we let $\Delta t = 10$ s, which is an almost instantaneous change compared to the time scale given by t_f.

As a result of the stress perturbation, an earthquake will nucleate at some time t_p., which will generally differ from t_f. The *clock advance* CA is defined as

$$CA = t_f - t_p. \tag{4.25}$$

Negative values of CA are also called *clock delay.*

4.3.1.1 Coulomb stress changes of varying amplitude

In this numerical experiment, we apply shear stress of increasing amplitude to the whole area of the fault and at a square with center coinciding with the center of the fault but with half the area (for simplicity we will refer to this area as the center half). We run the earthquake cycle 45 times for each amplitude. In each run, we apply shear stress at different time t_0 to study the dependence of clock advance on t_0. We increase $t_0$by 2 years in each subsequent run (for a given amplitude). The resulting graphs of clock advance vs t_0 are shown in figures 4.4 and 4.5 respectively. Let us describe their most outstanding features . First, each curve can be separated in three chronological phases - a flat (or static) phase, an oscillatory phase and an instant triggering phase.

The flat phase is observed for early times of applications. In this phase, there's a constant clock advance CA_0 that increases with the magnitude of ΔCS. We plot the dependence of the CA_0 - determined as the CA for ΔCS applied at the first year of the earthquake cycle - on the magnitude of ΔCS in figure 4.6. As we can see, for both areas of application the magnitude of the static phase depends linearly on ΔCS until it saturates at instant triggering. The slope is slightly steeper for the application to the whole fault. Thus, for applications early in the cycle, there is in agreement with the formulas for clock

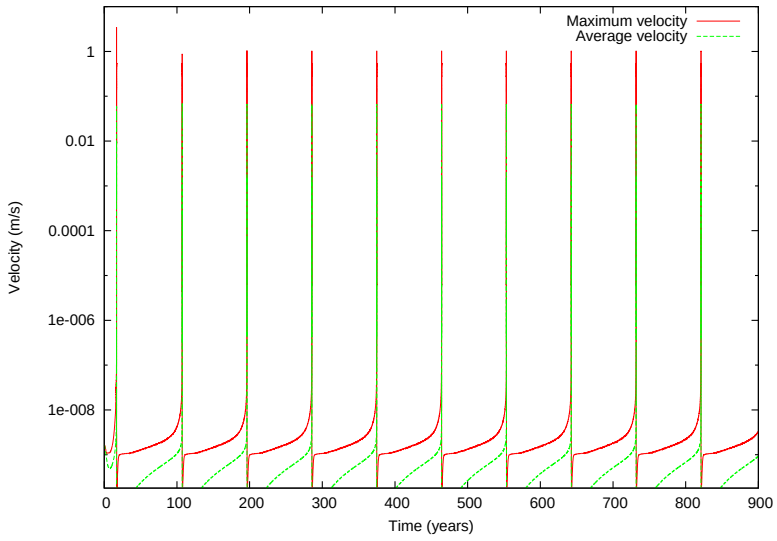

(a)

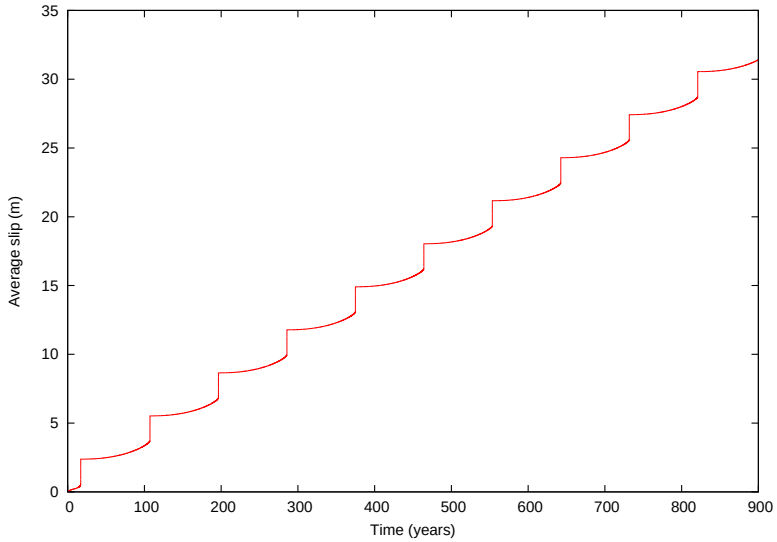

(b)

Figure 4.1: A graph of a) maximum (red) and average (green) velocity on the homogeneous fault, b) average slip on the fault

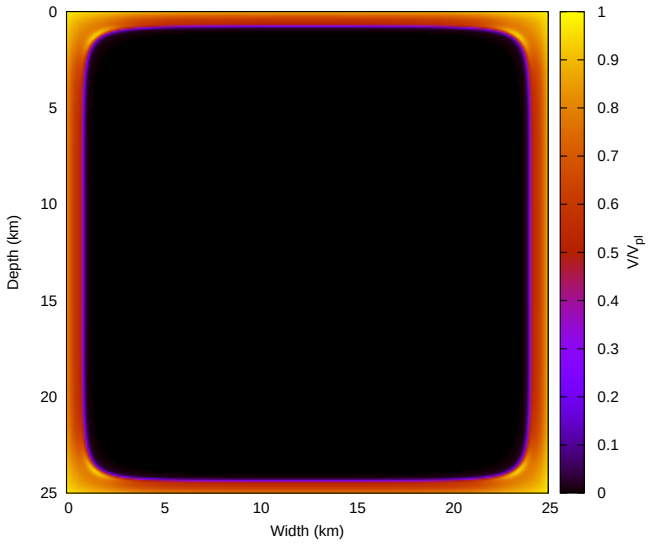

(a)

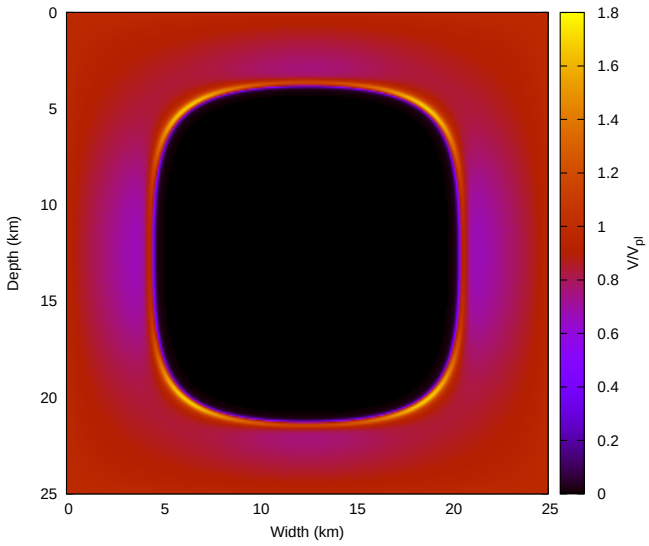

(b)

Figure 4.2: Snapshots of the velocity field at a) $t = 16$ years , b) $t = 72$ years (relative to the earthquake cycle)

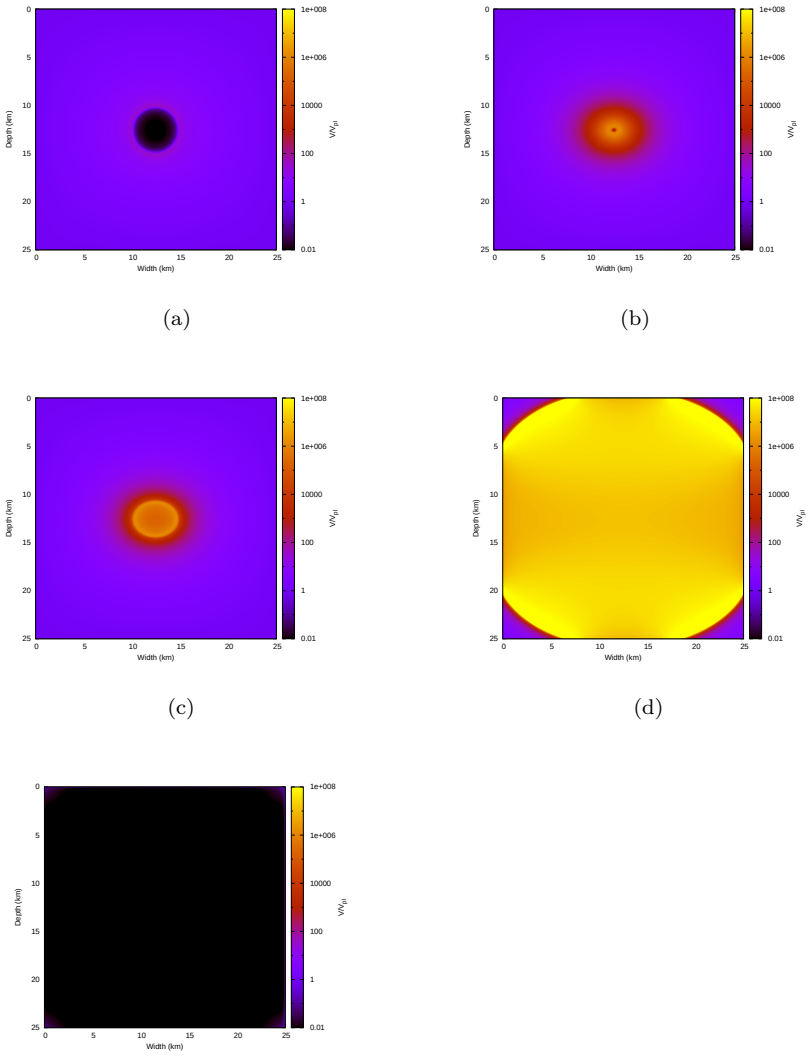

(a) (b)

(c) (d)

(e)

Figure 4.3: Various phases of the earthquake nucleation

advance (4.23) derived for the spring slider model, which also predict linear dependence of CA on $\Delta\tau$. However, the formula does not explain the difference in constants of proportionality for the two areas.

After the flat phase, an oscillatory phase begins, in which the values of CA oscillate around a mean that is close to CA_0. Note that for small values of ΔCS, the values of clock advance even sometimes go below zero during this phase - in other words, the earthquake has a delay even for positive ΔCS. The onset of the oscillatory phase decreases with the increasing ΔCS amplitude. Moreover, if we compare pictures 4.4 and 4.5, we can see that this onset comes much later for partial ΔCS application then for applications to the whole fault. This might suggest that onset of oscillations decreases with increasing application area. We explore this possibility in one of the next sections. The oscillations for the whole fault have a period of about 10 years. If we used the formula derived for oscillations of perturbations around steady-state value, then this would give an estimate of stiffness k_{oscil} of about hundred times k_{crit}. It does not seem that those oscillations could be the cause of the oscillations in clock advance seen here.

Finally, except for the smallest values of ΔCS (0.2% and 0.3% of σ_0), the oscillatory phase transitions to instantaneous triggering - for a given magnitude of ΔCS, there's a time after which positive Coulomb stress application causes earthquake to begin immediately. Once an earthquake is triggered instantly for some t_0, it is triggered instantly for all subsequent times $t > t_0$. For ΔCS large enough, this instantaneous phase even starts at the beginning of cycle, so neither the flat nor the oscillatory phases are observed.

In figure 4.7 we show a comparison of one chosen CA curve with the clock advance predicted by the spring slider formula 4.23. We used the estimate of stiffness k for rectangular fault and $\dot{\delta}(0)$ is calculated from eq. 1.59, so that the prediction for the free interseismic period t_f matches the observed one. We can see that the formula overestimates the real clock advance at the beginning of the earthquake cycle and underestimates it near the end.

4.3.1.2 Response to negative values of ΔCS

Let us take a look at the effect of negative Coulomb stress application (unloading) and compare them with positive applications of the same amplitude . We choose six different values of ΔCS: $\pm 0.001\sigma_0$, $\pm 0.01\sigma_0$ and $\pm 0.1\sigma_0$ and we apply stress to the whole fault and to its central half. The results for the negative values are shown in figure 4.8. As we can see, the qualitative features for the negative ΔCS curves are almost the same as for the positive ones, but there is no instantaneous triggering The flat phase of CA is negative, i.e. there's a clock delay. However, for the smaller values of ΔCS, the CA is positive for certain times of application during the oscillatory phase. In figure 4.9, we compare the absolute values CA for positive and negative values of ΔCS with the same absolute value. As we can see, the absolute values of CA in the flat phases exactly match - i.e. the values of CA_0 for loading and unloading are symmetrical around zero. Also, the onset of the oscillatory phase begins at the same time for

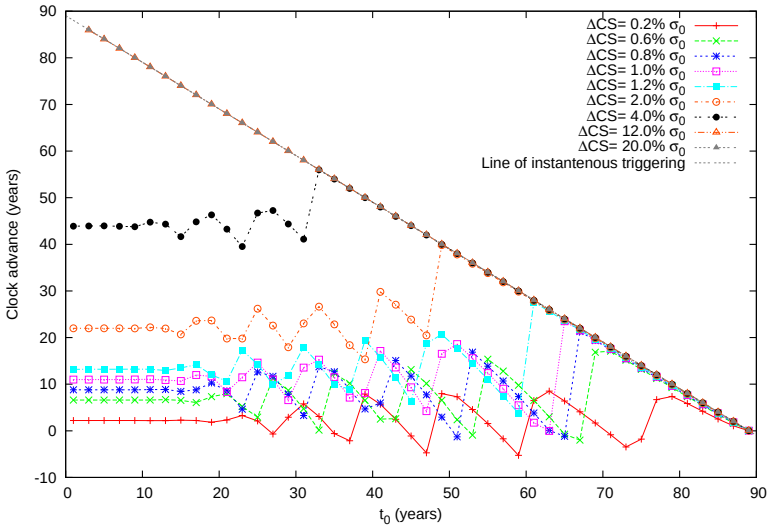

Figure 4.4: Clock advance vs t_0 for increasingly large amplitudes of ΔCS to the area of whole fault.

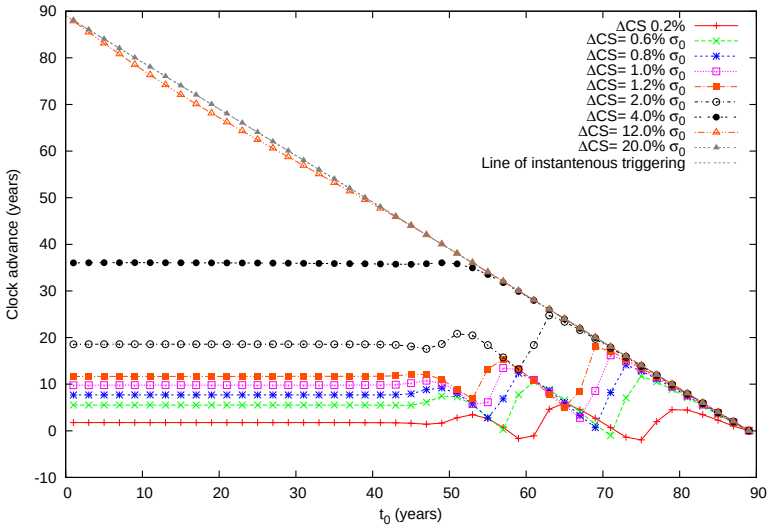

Figure 4.5: Clock advance vs t_0 for increasingly large amplitudes of ΔCS to the center half of the fault.

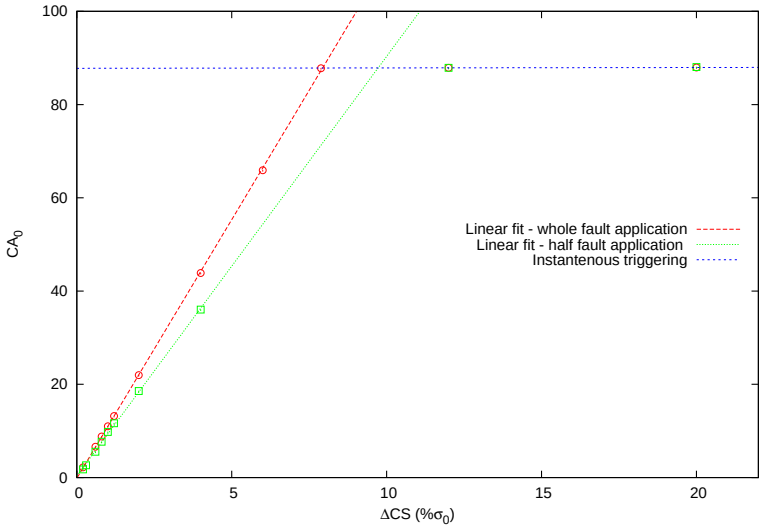

Figure 4.6: CA_0 vs ΔCS for application of Coulomb stress to the whole fault (red) and to its center half (green). Linear fits are drawn by red and green dashed curves. The blue line is the clock advance corresponding to instantaneous triggering.

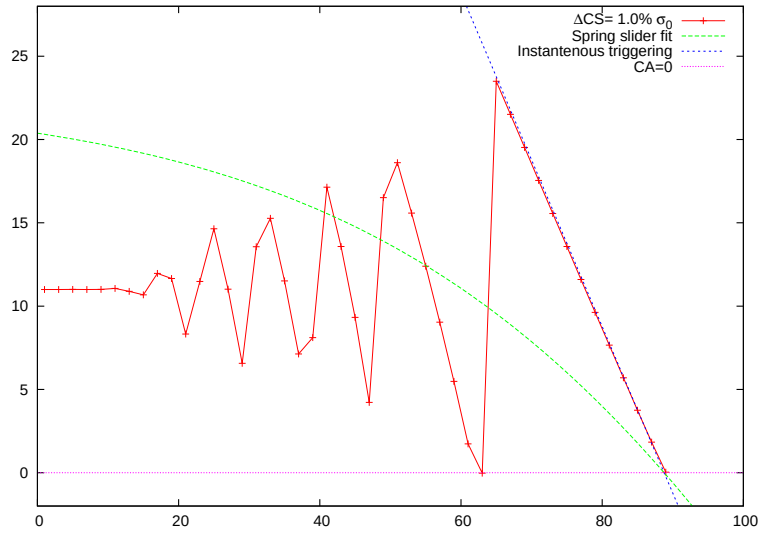

Figure 4.7: A fit of the spring slider formula (4.23) to the clock advance corresponding to a application of $\Delta CS = 1\%$ to the whole fault. See text for details

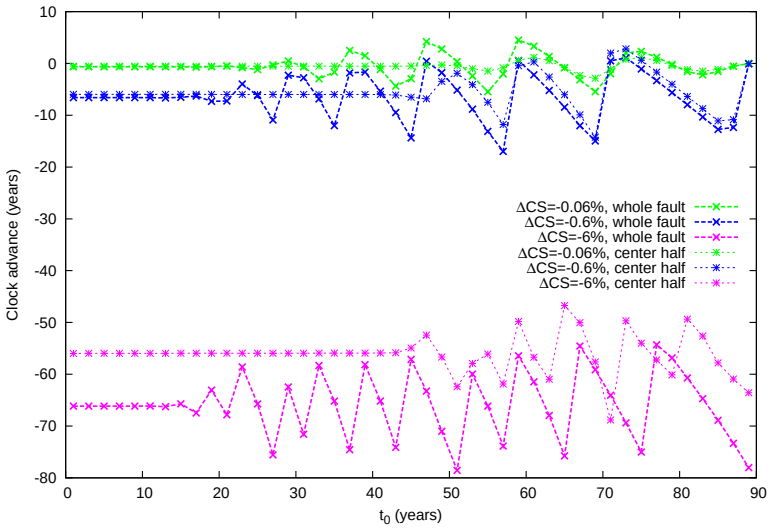

Figure 4.8: Clock advance for negative values of ΔCS. The thin and bold lines signify applications of ΔCS to the whole fault and its center half, respectively, while same colors correspond to same values of ΔCS.

loading and unloading. During the oscillatory phase itself, the absolutes values may differ up to an order of 10.

4.3.1.3 Comparison between applications of normal vs shear stress

Here, we compare clock advance for equivalent values of ΔCS, but realized with either shear or normal stress. We use the notation $\Delta CS(\Delta\tau, \Delta\sigma) = \Delta\tau - \mu_* \Delta\sigma$ to distinguish between the two cases, so that $\Delta CS(\Delta\tau, 0)$ corresponds to a pure shear stress change and $\Delta CS(0, \Delta\sigma)$ to a pure normal stress change. We again use six different values of ΔCS: $\pm 0.001\sigma_0$, $\pm 0.01\sigma_0$ and $\pm 0.1\sigma_0$ and apply stress to the whole fault (we also performed the test for the center half with same qualitative results). The resulting graphs of CA vs t_0 are shown in figure 4.10 for positive ΔCS and figure (4.11) for negative ΔCS. As we can see, for the smaller absolute values of ΔCS, the corresponding curves (for which $\Delta CS(\Delta\tau, 0) = \Delta CS(0, \Delta\sigma)$) match each other very closely. However, for the $|\Delta CS| = 0.1\sigma_0$ curves, there is a small difference at the beginning (before both curves change to instant triggering). This is in agreement with what one might expect from equations of the system - if $\Delta\sigma$ is small in comparison toσ then $\Delta\tau$ and $\Delta\sigma$ appear in the combination $\Delta\tau - \mu_* \Delta\sigma$, which is equal to ΔCS for small deviations of $\mu(t)$ from μ_*. For larger values of $\Delta\sigma$, the term in denominator,

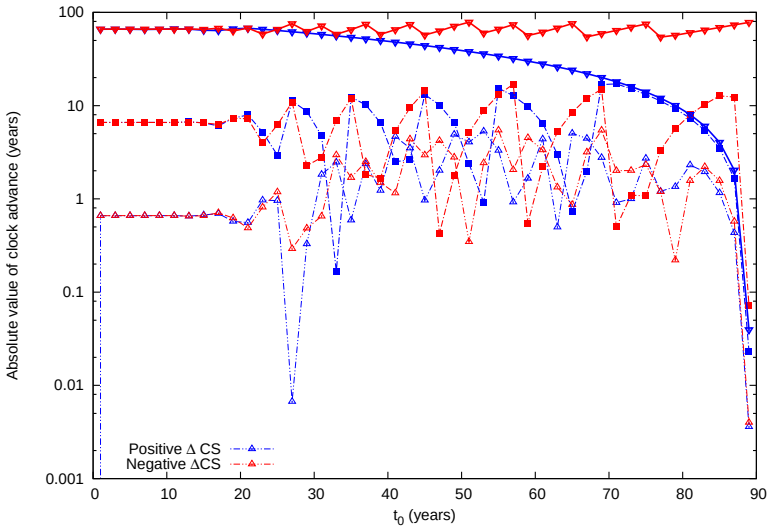

Figure 4.9: Comparison of absolute values of CA for applications of ΔCS with same absolute values but opposing signs. Three values of $|\Delta CS|$ ($0.006\sigma_0$, $0.06\sigma_0$ and $0.6\sigma_0$) are used.The blue lines represent positive ΔCS application, while the red lines represent negative applications. Log-scale is used for better visibility.

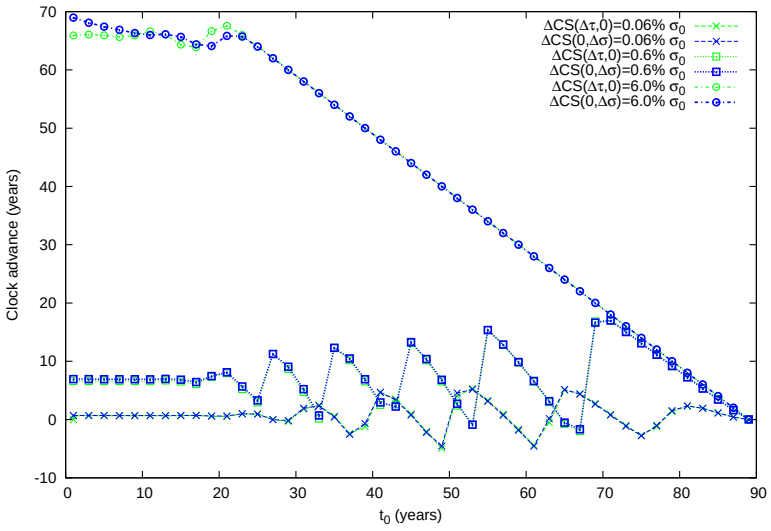

Figure 4.10: Clock advance resulting from applying either the shear stress $\Delta\tau$ or normal stress $\Delta\sigma$ whose amplitudes give the same value of $\Delta CS(\Delta\tau, \Delta\sigma)$. Positive ΔCS is applied.

the deviations of $\mu(t)$ from μ_* or the last term in 1.30 cause the asymmetric response. However the difference in average values of CA is not large, neither quantitatively nor qualitatively, we therefore do not distinguish between ΔCS realized by normal or shear stress.

4.3.1.4 The effect of ΔCS pulse time

In the above numerical experiments, ΔCS was applied in a duration of $\Delta t = 10$ s. Compared to the inter-seismic period of 90 years, this is essentially a step-change. We saw that this application result in the presence of an oscillatory phase, whose period is about 10 years. We were interested whether applying ΔCS for longer times might make the oscillations disappear. For this reason, we applied shear stress for $\Delta t = 10$ years (even though such slow changes of $\Delta\tau$ are not realistic) instead of 10 seconds, while keeping the total ΔCS constant. The comparison of the resulting CA curves with the ones from $\Delta t = 10$ s application is shown in figures 4.12 (for applications to the whole fault) and 4.13 (center half). Remarkably, the value of the static phase CA_0 is insensitive to the pulse duration and depends only on the total ΔCS. It turns out that the oscillations are preserved even for the large Δt. In the case of whole fault applications, the periods of oscillations for $\Delta t = 10$ years are somewhat longer

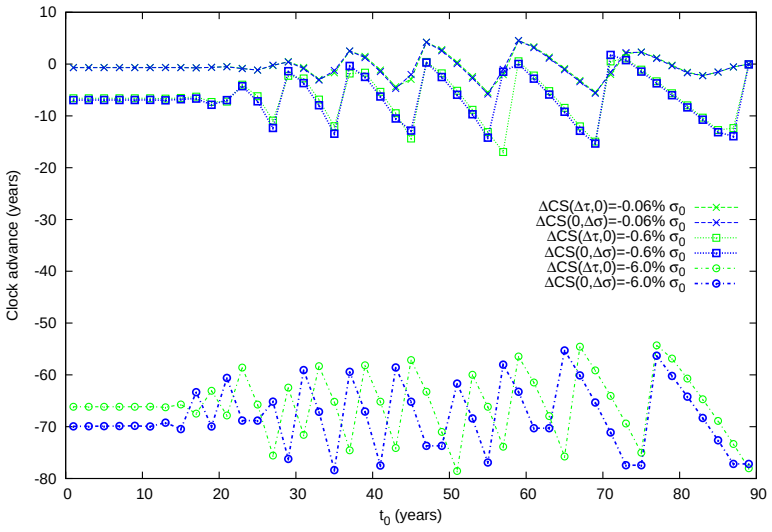

Figure 4.11: Clock advance resulting from applying either the shear stress $\Delta\tau$ or normal stress $\Delta\sigma$ whose amplitudes give the same value of $\Delta CS(\Delta\tau, \Delta\sigma)$. Negative ΔCS is applied

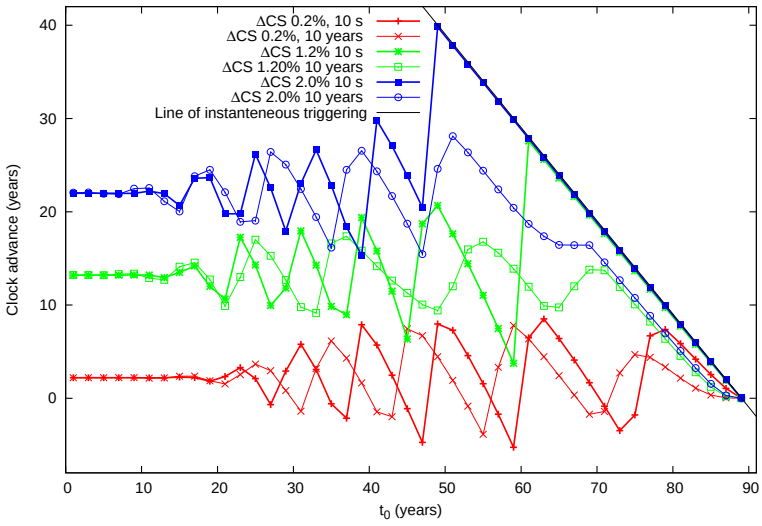

Figure 4.12: Comparison of CA for $\Delta t = 10$ s (bold) and $\Delta t = 10$ years (thin). ΔCS was applied to the whole fault.

(we can see observe one more local maximum than in the $\Delta t = 10$ s case), but the different is not significant. The onsets of the oscillations are very close to each other in the case of the whole fault, but have a "phase shift" of about 5 years in the case of the center half application. The instantaneous phase is missing for the 10 years pulse, which is understandable, because the injection is not applied instantaneously so the "instantaneous triggering" does not even make much sense in this case .

4.3.1.5 Dependence of CA on the area of Coulomb stress load

An interesting question regarding the effect of Coulomb stress loading, which cannot be answered with the spring slider model, is the role of the area over which it is applied. Is the resulting CA affected by it, or is amplitude (e.g. maximal amplitude) all that matters? Is the integral of ΔCS over the fault area an important factor? To explore this question, we applied Coulomb stress to squares of varying area. Since changing the application area obviously also changes the localization of Coulomb stress, we place the squares on different places on the fault - one set was placed at the center, one in the corner and touched the fault's edge. The graph of CA vs $t_0$for different areas is plotted in figure 4.14, the graphs for the edge squares are in figure 4.15. We can see that curves with larger area have higher mean values of CA (i.e. CA is greater

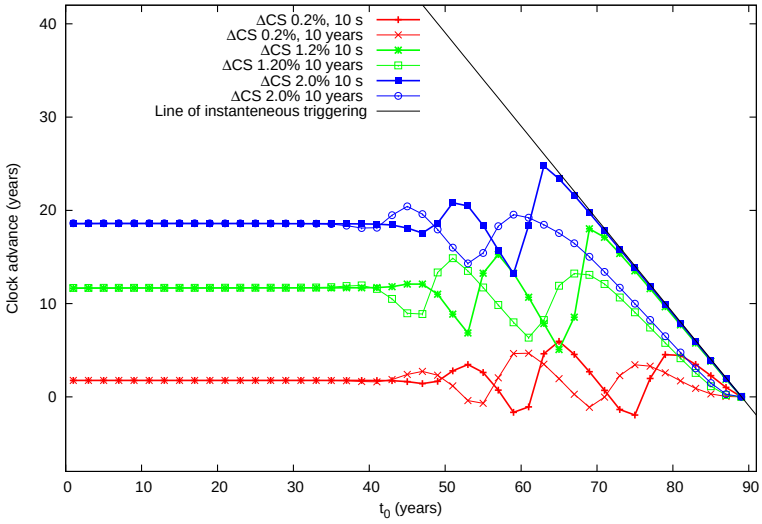

Figure 4.13: Comparison of CA for $\Delta t = 10$ s (bold) and $\Delta t = 10$ years (thin). ΔCS was applied to the center half of fault.

on average), but this may occasionally even be lower during oscillatory phase. The graph of CA_0 vs area for the three square locations is in figure 4.16. CA_0 clearly is an increasing function of areas, but not a linear one. We can also see that the dependence of CA_0 on area differs with the application location. An interesting feature for the center square application (fig. 4.14) is that the onset of CA oscillations seems to depend on the application area - it starts earliest for the whole area application and latest for the 1/3 area application. However, this is not true for the case of edge applications (fig. 4.15). Thus the location of ΔCS, not area, must be the cause of this behavior. We confirmed this by only applying ΔCS to edges of the squares - the onset of oscillations was then the same as for the whole squares. We believe that this influence can be explained by evolution of velocities on the fault.

4.3.1.6 Application of normalized Coulomb stress and explanation of the oscillations

The term in derivative proportional to $\Delta\dot{\tau}$ has a term in derivative which term. We suspect that the oscillations on fault are caused by this term. To shed some light upon this issue, we applied Coulomb stress normalized so that each cell on the fault experiences the same change in velocity. This amounts to multiplying the amplitude ΔCS_i applied to cell c_i with factor f_i equal to

$$f_i = \frac{\frac{a\sigma}{V_i}+\eta}{\frac{a\sigma}{V_0}+\eta}, \tag{4.26}$$

where V_0 is a velocity of choice. This changes dV_i/dt to

$$\frac{dV_i}{dt} = \ldots + \frac{\Delta\tau}{\frac{a\sigma_0}{V_0}+\eta}, \tag{4.27}$$

where the ellipses denote term independent of $\Delta\tau$. We choose this to be the velocity at the center of the fault. The resulting clock advance is in figure 4.17.

We believe the explanation for oscillations can be explained by looking at fig. 4.2 . We can see that there is a circular "wavefront" of high velocities, which converges to the middle (when that happens a nucleation occurs, which is plotted in figure 4.3). The velocities inside the converging wavefront are very small when compared to V_{pl} ($V/V_{pl} \approx 10^{-4}$). The velocities behind the wavefront are somewhat smaller than V_{pl}, while $V = V_{pl}$ at the rest of the fault. We believe that this propagation explains the oscillations and why their onset begins later for applications to smaller areas with centers at the center of fault. For smaller times, if the ΔCS is applied inside the “black”, low-velocity area, then the term in derivative proportional to $\Delta\dot{\tau}$ is proportional to velocity and is constant when plotted against t_0. As the wavefront passes the area of ΔCS application, the term starts to vary in time and oscillations begin. For example, we estimate that the front passes the center half at about 53 years which is close to the onset of oscillations seen in figure 4.5. This is an alternate explanation to that of Perfettini (2003), who speculated that oscillations in velocity caused

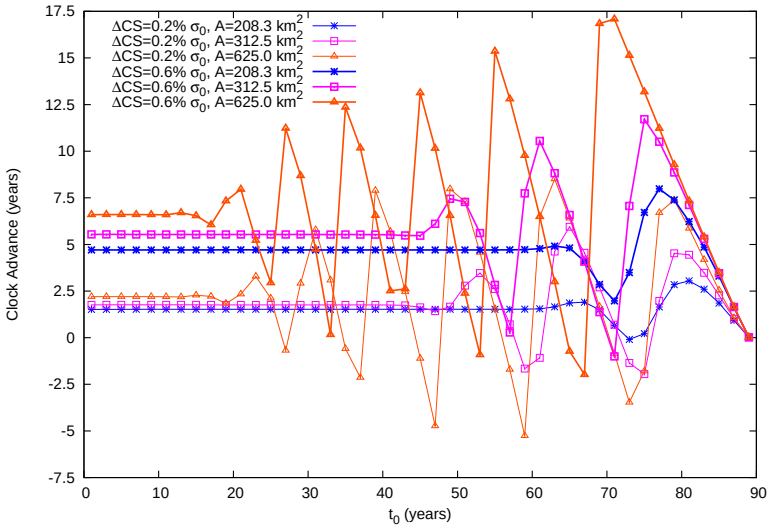

Figure 4.14: CA for two amplitudes and three squares of different area with centers coinciding with the center of the fault. The curves belonging to the same area are distinguished by color and amplitudes are distinguished by line thickness.

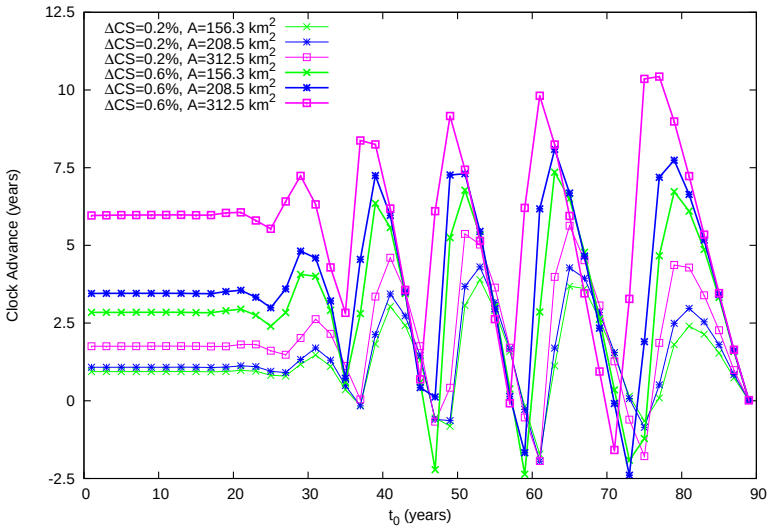

Figure 4.15: CA for two amplitudes and three squares of different area at the edge of fault. The curves belonging to the same area are distinguished by color and amplitudes are distinguished by line thickness.

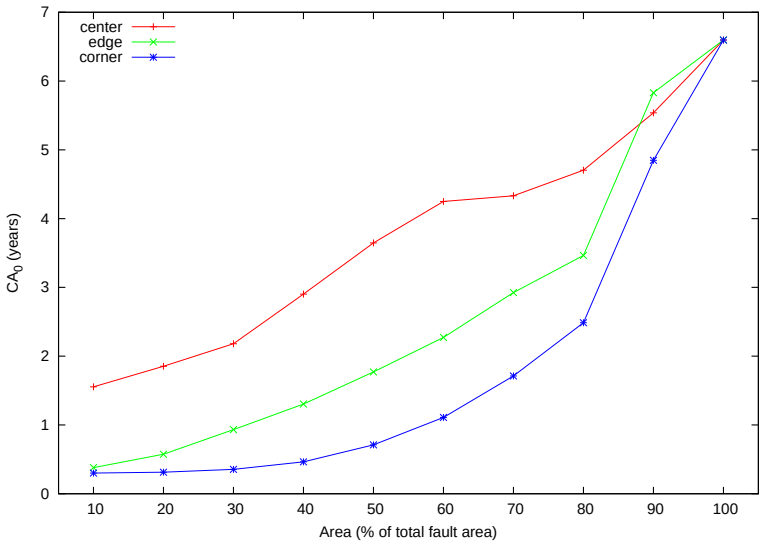

Figure 4.16: Dependence of the static clock advance CA_0 on total Coulomb stress load area for three different locations on fault. A Coulomb stress of constant amplitude equal to 0.2% of σ_0 is applied.

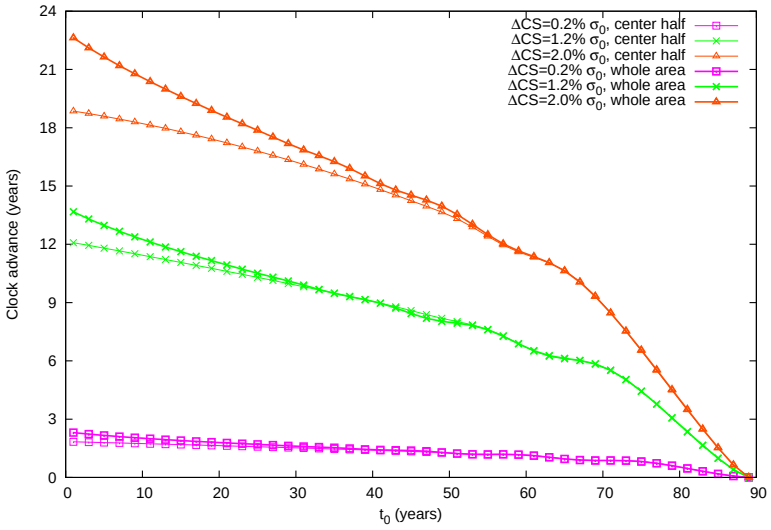

Figure 4.17: Clock advance vs time for Coulomb stress normalized to give constant acceleration. CS applied on the whole fault.

by ΔCS would die out before having a tangible effect on clock advance. We believe that due to the low effect of ΔCS application in the low velocity zone, no velocity oscillations are excited at all. This propagation effect also explains why no oscillatory phase is visible in the one-dimensional spring slider model.

4.3.2 Heterogeneous fault

We performed numerical experiments on clock advance on a model of heterogeneous fault with a random distribution of D_C that produces Gutenberg-Richter seismicity with $b = 1$ in a range of about 2 magnitudes. This is the fault whose seismicity was shown in figure 3.3 in chapter 3. The fault has dimensions of $35 \times 35\ km^2$ discretized into 128×128 cells and it has zero dip (it is a strike-slip fault). The bottom edge of the fault is in the depth of 35 km, so the top edge lies on the free surface. The distribution of parameters a and $a-b$ in this model is shown in figures 4.18 and 4.19. The depth dependence prescribed in the interval of 3.5 km to 31.5 km along the fault strike is a standardly used distribution taken after Blanpied et al. (1991), linearly scaled to the depth of 35km. We plot this dependence (in terms of parameters a and $a-b$) in figure 4.20. There are velocity strengthening regions at the top and bottom of the fault, and a velocity-weakening (seismogenig) zone at the center. Near the verticals edges, there's a linear transition from this distribution $a_{Blanpied}$ to $a = 1.5 \times a_{Blanpied}$ and $b = 0$. This transition is used to stabilize the fault near the vertical edges. The distribution of D_C is in figure 4.21. The bottom 5 km have a constant value of $D_C = 0.3$ km (but this value is not important, because $b = 0$ in this depth range). The distribution on the rest of the fault was obtained by using a uniform initial distribution of parameters and using the filters described in subsection 3.0.3 with $N = 0$, $c = 0.82$ km and $a_G = 0$. The mean value of D_C is 0.03 m, and it ranges from 0.01 m to 0.05 m. The value of other parameters is the same as for the homogeneous fault: $\mu_* = 0.6$, $\alpha = \mu_*/3 = 0.2$, $V_* = 10^{-6}$ m, $\sigma_0 = 75$ MPa, $\lambda = 20$ GPa, the shear modulus $\mu = 30$ GPa, $\beta = 3$ km/s and $V_{pl} = 3.5$ cm/year.

For numerical experiments with clock advance, we chose the cycle from figure 3.3 which starts at 518.7 years and, when unperturbed by Coulomb stress, has events occurring at 587.7 years. The inter-seismic time for this cycle is thus 69.0 years. We performed a small number of experiments similar to the case of homogeneous fault - we tested the response to Coulomb stress change of different magnitudes and compared the absolute values of CA for positive and negative Coulomb stress changes. The results are presented below.

4.3.2.1 Results

The graph of CA vs t_0 for several amplitudes of ΔCS applied to the whole fault can be seen in figure 4.22. As we can see, the response of the model is qualitatively the same as that of the homogeneous fault - the dependence of clock advance on time can still be separated in the static, oscillatory and the instantaneous triggering phases. In figure 4.23 we show the dependence of the

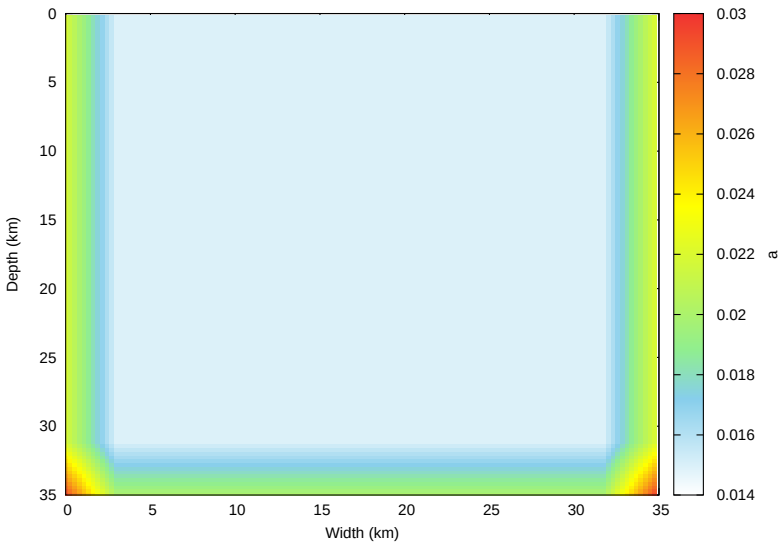

Figure 4.18: Spatial distribution of the frictional parameter a.

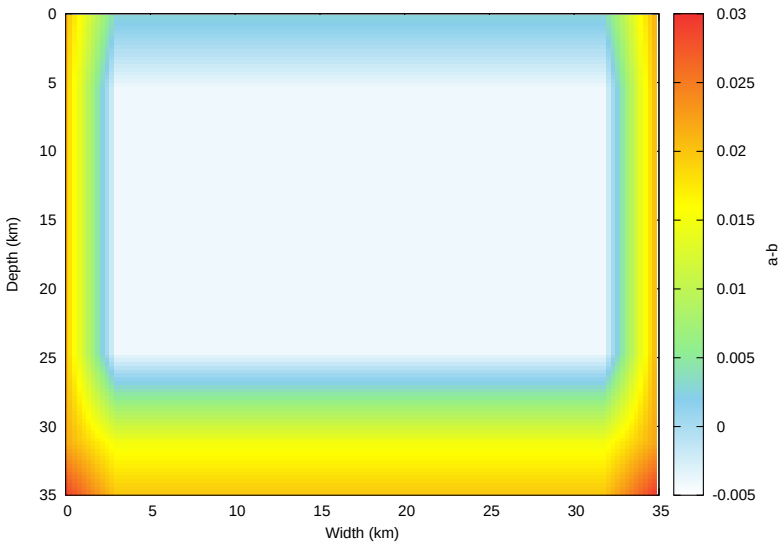

Figure 4.19: Spatial distribution of $a - b$.

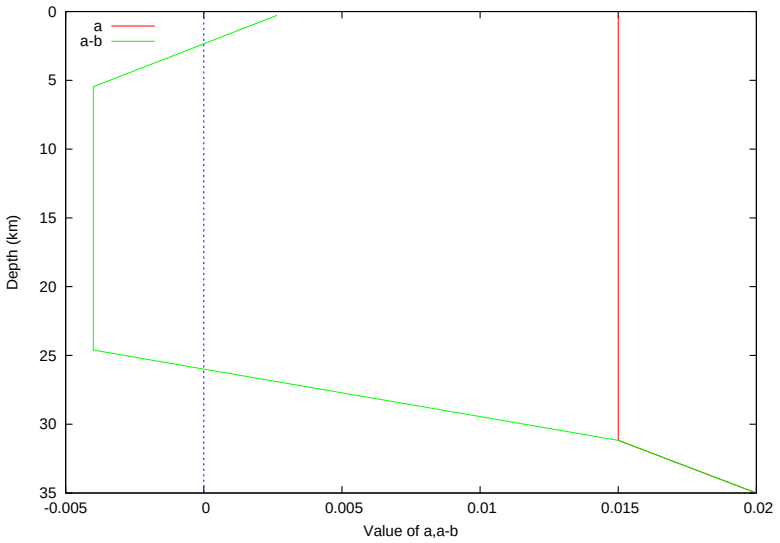

Figure 4.20: Depth dependence of parameters a and $a - b$ at width 12.5 km.

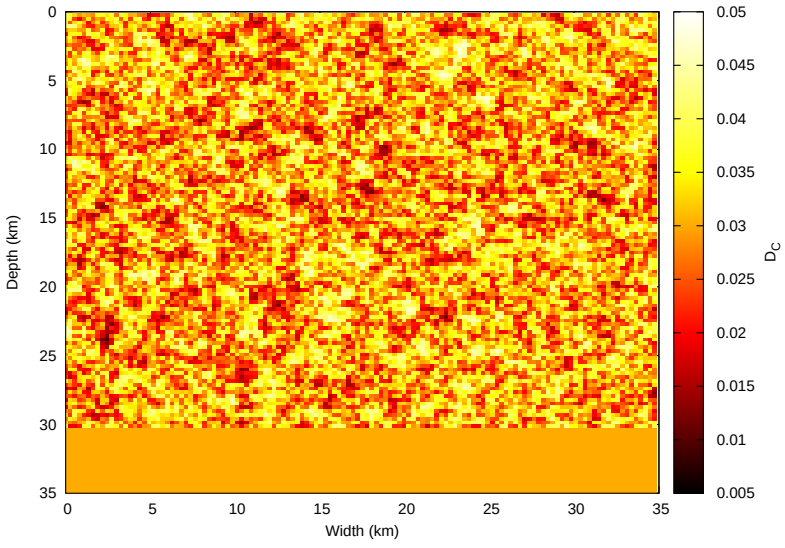

Figure 4.21: Spatial distribution of the parameter D_C.

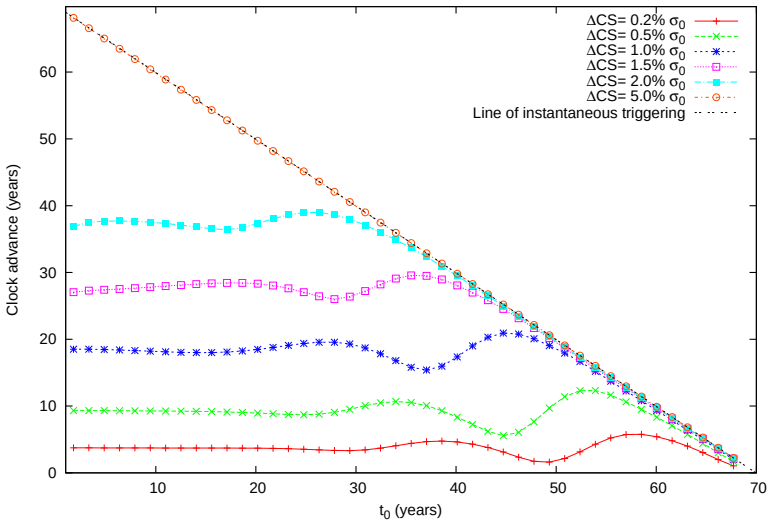

Figure 4.22: CA vs t_0 for increasingly large amplitudes of ΔCS to the area of whole fault.

amplitude of the static phase CA_0 on amplitude of Coulomb stress change for three areas of ΔCS application - the whole fault, one half and one quarter of the fault area. Like in the case of the homogeneous fault, CA_0 depends linearly on the ΔCS amplitude and the slope of the dependence is steeper for larger application areas. We also calculated CA for negative values of ΔCS and found that they produce clock delay (negative values of clock advance). The absolute values of CA in the static phase for applications of ΔCS with the same absolute value but opposite signs are the same, although they differ in the later phases - as was the case for the homogeneous fault. This is shown in figure 4.24. Overall, based on the results of these numerical experiments, we did not find any significant qualitative differences between clock advance behavior of the two models.

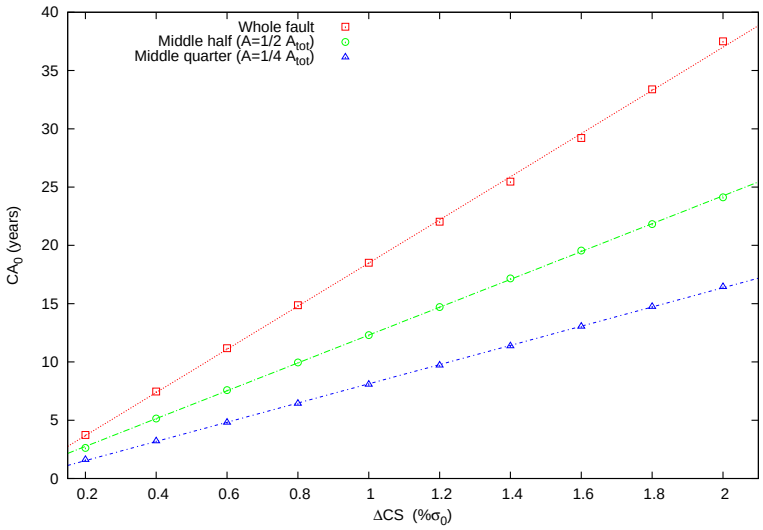

Figure 4.23: CA_0vs ΔCS for application of Coulomb stress to the whole fault (red), to its center half (green) and center quarter (blue). Linear fits are drawn with dashed lines.

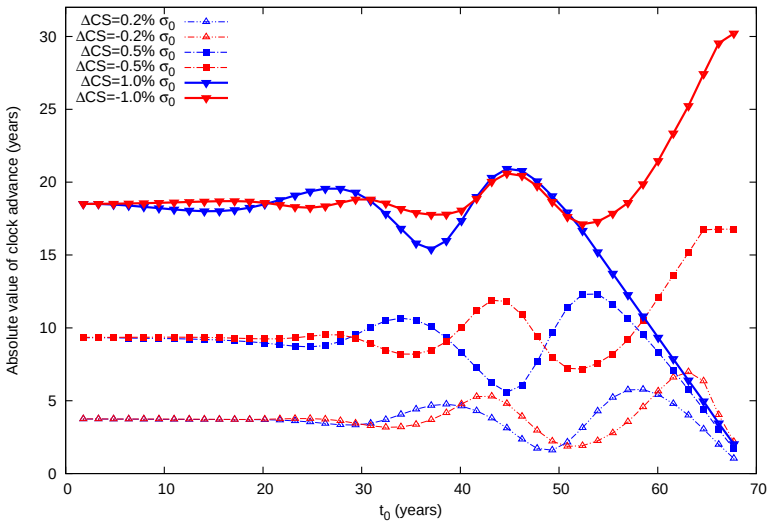

Figure 4.24: Comparison of absolute values of CA for applications of ΔCS with same absolute values, but opposing signs. Three values of $|\Delta CS|$ ($0.002\sigma_0$, $0.005\sigma_0$ and $0.01\sigma_0$) are used. The blue lines represent positive CS application, while the red lines represent negative applications.

Conclusion

In the first chapter of the thesis, we provided a theoretical background for modeling slip on a tectonically loaded fault governed by rate-and-state friction. We described the phenomenon of stick-slip using a model of Coulomb friction and explained the importance of friction for behavior of tectonic faults. We described the experiments on friction between rocks and presented the rate-and-state friction laws that were introduced to explain those experiments. We showed some basic properties of the rate-and-state laws and gave an alternate derivation for the formula of critical stiffness in the massive spring-slider , which governs the transition between stable and unstable sliding.

In chapter 2, we presented a numerical formulation for modeling the behavior of planar faults with rate-and-state friction. We made an approximation of quasi-dynamicity, in which fully dynamic contributions for stress are replaced with a radiation damping term proportional to slip velocity.

In chapter 3, we studied the effect of parameter distribution on seismicity. Despite the large number of models we tested, we did not find any systematic dependence of frequency-size distribution on the frictional parameters used, except for the influence of discretization. If power law behavior was found, then it was always in a limited range of at most two magnitudes. The reason why power law behavior is limited in range is because the rate-and-state models we used is unable to produce events with magnitude below a certain (model dependent) value. As far as the effect of discretization is concerned, we confirmed a result by previous authors that discrete models with cells that are able to fail independently of one another, easily produce power law behavior in a limited range. The sparser discretization used, the steeper is the slope of the frequency-size distribution. Moreover, the character of events produced in this manner is such that events of smaller magnitude and size are temporally clustered around the larger events. We can think of two ways in which more realistic seismicity might be achieved - 1) using distributions with parameters ranging over wider scales and 2) using a fully dynamic model.

In chapter 4, we studied the effect of Coulomb stress change ΔCS on clock advance CA of seismic cycles in various times of applications t_0. We performed a number of numerical experiments studying the effects of both positive and negative ΔCS amplitude, extent and position of the load area, duration, and so on. For both the homogeneous and heterogeneous models, we observed the behavior described before by Perfettini (2003) and Gallovič (2008), who found

that dependence of CA on t_0 can be separated in three phases - a static one, during which the clock advance has a constant value regardless of t_0, an oscillatory one and a phase of instantaneous triggering. We found that the mean clock delay scales with amplitude of ΔCS for homogeneous applications, but the constant of proportionality depends on the area of ΔCS application. We suggested that the origin of the oscillations is due to propagation effects of slip velocity in the model. This is supported by the fact that no oscillations are present in a simple spring slider model. Another reason why we believe that the oscillations are caused by distributions of slip velocity is that the oscillations can be made to disappear by using a heterogeneous distribution of Coulomb stress, realized so that it causes the same acceleration for each point on the fault, regardless of its velocity. On the other hand, when the Coulomb stress is applied over a long time, the oscillations do not disappear. Proper understanding of the observed effects requires further study.

Bibliography

[1] Beeler, N.M., T. E. Tullis, and J. D. Weeks (1994). The roles of time and displacement in the evolution effect in rock friction, Geophys. Res. Lett., 21, 1987-1990

[2] Berman, A., Drummond, C., and Israelachvili, J. (1998). Amontons' law at the molecular level. Tribol. Let., 4:95–101.

[3] Bhattacharya, P.; Rubin, A. M.; Bayart, E.; Savage, H. M.; Marone, C.; Beeler, N. M. (2013). Experimental and Analytical Evaluation of Stressing-Rate State Evolution in Rate-State Friction Laws, American Geophysical Union, Fall Meeting 2013, abstract

[4] Blanpied, M. L., D. A. Lockner, and J. D. Byedee (1991), Fault stability inferred from granite sliding experiments at hydrothermal conditions, Geophys. Res. Lett., 18(4), 609-612, 1991.

[5] Brace,W. F. & Byerlee (1966). J. D. Stick slip as a mechanism for earthquakes. Science 153, 990–992 .

[6] Dieterich, J. H. (1979). Modeling of rock friction: 1. Experimental results and constitutive equations, J. Geophys. Res., 84(B5), 2161–2168, doi:10.1029/JB084iB05p02161

[7] di Liberto (2015). Stick-Slip Dynamics: Oscillations with Friction for undergraduates Francesco di Liberto, http://www.researchgate.net/publication/228942296_Stick-Slip_Dynamics_Oscillations_with_Friction_for_undergraduates

[8] Elmer, F-J. (1997). Nonlinear Dynamics of Dry Friction, arXiv:chao-dyn/9707004

[9] Gallovič, F. (2008). Heterogeneous Coulomb stress perturbation during earthquake cycles in a 3D rate-and-state fault model, Geophys. Res. Lett., 35, L21306, doi:10.1029/2008GL035614

[10] Gu, J.-C., J. R. Rice, A. L. Ruina, and S. T. Tse (1984). Slip motion and stability of a single degree of freedom elastic system with rate and state dependent friction, J. Mech. Phys. Solids, 32, 167 – 196.

[11] Hillers, G., Y. Ben-Zion, and P. M. Mai (2006). Seismicity on a fault controlled by rate- and state dependent friction with spatial variations of the critical slip distance, J. Geophys. Res., 111, B01403, doi:10.1029/2005JB003859

[12] Kato, N. (2004). Interaction of slip on asperities: Numerical simulation of seismic cycles on a two-dimensional planar fault with nonuniform frictional property, J. Geophys. Res., 109, B12306, doi:10.1029/2004JB003001.

[13] Klimeš L. (2002), Correlation Functions of Random Media, Pure appl. geophys. 159 (2002) 1811–18310033 – 4553/02/081811 – 21 $ 1.50+ 0.20/0

[14] Lapusta, N, Rice, J. R.,Ben-Zion, Y., Zheng, G. (2000). Elastodynamic analysis for slow tectonic loading with spontaneous rupture episodes on faults with rate- and state-dependent friction J. Geophys. Res,105(B10),23765-23789,doi:10.1029/2000JB900250

[15] Lapusta, N., Bardot, S (2012). The mechanics of Faulting: From Laboratory to Real Earthquakes Linker, M.F., and Dieterich, J.H. (1992). Effects of variable normal stress on rock friction: Observations and constitutive relations, J. Geophys. Res. , 4923-4940.

[16] Morgan Page and Karen Felzer (2015). Southern San Andreas Fault seismicity is consistent with the Gutenberg-Richter magnitude-frequency distribution

[17] Nagata, K., M. Nakatani, and S. Yoshida (2012). A revised rate- and state-dependent friction law obtained by constraining constitutive and evolution laws separately with laboratory data, J. Geophys. Res., 117, B02314, doi:10.1029/2011JB008818.

[18] Nakatani, M., Mochizuki, H. (1996). Effects of shear stress applied to surfaces in stationary contact on rock friction Geophysical Research Letters,23(8),869-872 DOI: 10.1029/96GL00726

[19] Newman, M. E. J. (2004). Power laws, Pareto distributions and Zipf's law, arXiv:cond-mat/0412004 Bulletin of the Seismological Society of America

[20] Nordhagen, H. (2003). Stick-Slip Friction, PhD. thesis, Hovedoppgave, University of Oslo, 2003

[21] Paterson, M.S., Teng-fong Wong (2005), Experimental Rock Deformation - The Brittle Field, Springer Science & Business Media

[22] Perfettini, H., J. Schmittbuhl, and A. Cochard (2003). Shear and normal load perturbations on a two-dimensional continuous fault: 2. Dynamic triggering, J. Geophys. Res., 108, 2409, doi:10.1029/2002JB001805, B9.

[23] Putelat, T., Dawes, J. H. P. and Willis, J. R. (2011). On the micro-physical foundations of rate-and-state friction. Journal of the Mechanics and Physics of Solids, 59 (5), pp. 1062-1075.

[24] Rabinowicz, E. (1951). The Nature of the Static and Kinetic Coefficients of Friction, J. Appl. Phys., 22, 1373-1379.

[25] Rice, J.R., Ruina, A. L. (1983). Stability of Steady Frictional Slipping, Journal of Applied Mechanics, vol. 50, pp. 343-349 Zoback, ML. (2006). The 1906 earthquake and a century of progress in understanding earthquakes and their hazards, GSA Today: v. 16, no. 4/5, doi: 10.1130/GSAT01604.1